Temporal patterns of greenhouse gas emissions from two small thermokarst lakes in Nunavik, Canada

Amélie Pouliot[1,3]; Isabelle Laurion [2,3]; Antoine Thiboult [1]; Daniel F. Nadeau [1]

[1]Department of Civil and Water Engineering, Université Laval, Québec, Qc
[2]Centre Eau Terre Environnement, Institut national de la recherche scientifique, Québec, Qc
[3]Centre d'études nordiques, Université Laval, Québec, Qc

Correspondence: Amélie Pouliot (amelie.pouliot.1@ulaval.ca) and Daniel Nadeau (daniel.nadeau@gci.ulaval.ca)

Abstract. Small thermokarst lakes, formed by the thawing of ice-rich permafrost, are significant sources of greenhouse gases (GHG). Most estimates of emissions rely solely on daily measurements, which may bias annual flux calculations. In this study, we combined GHG flux measurements from two intensive summer campaigns with nearly two years of continuous temperature, oxygen, and conductivity profiling in two small (<200 m^2) thermokarst lakes in Nunavik (56°33'28.8"N, 76°28'46.5"W), Canada. One campaign occurred during a colder period (8.8°C average temperature) and the other during a warmer one (14.6°C average temperature), with one lake being humic and sheltered and the other more transparent and wind-exposed. Average diffusive fluxes of CO_2 (22.1 ± 20.5 mmol m^{-2} d^{-1}; mean ± standard deviation) and CH_4 (14.3 ± 14.2 mmol CO_2-eq m^{-2} d^{-1}) were consistent with values reported for similar thermokarst lakes, while N_2O fluxes were negligible (–0.8 ± 1.3 mmol CO_2-eq m^{-2} d^{-1}). Emissions increased 4-fold during the warmer summer, alongside the emergence of a diel trend, where daytime (09:00-17:00) CO_2 fluxes increased by 47%, CH_4 by 95%, and negative N_2O fluxes by 75% relative to nighttime fluxes. Moreover, ebullitive CH_4 fluxes were six times higher than diffusive fluxes in the humic, sheltered lake, reaching 117.0 ± 44.7 mmol CO_2-eq m^{-2} d^{-1}. Seasonal flux estimates indicate that emissions could peak in fall and spring, as the lakes accumulated large concentrations of GHG at the bottom. Our findings highlight the importance of including both daytime and nighttime measurements, as well as storage fluxes (emitted in spring and fall), to improve the accuracy of GHG emission estimates from thermokarst lakes.

1 Introduction

Permafrost thaw in ice-rich soils results in the formation of thermokarst lakes, which vary widely in size–from a few hundred square meters to over 50 square kilometres. These lakes, common across Arctic and subarctic regions of Siberia, Alaska, and Canada, differ from other northern lakes in their mixing regime, transparency, and biogeochemistry (e.g., Sepulveda-Jauregui et al., 2015; Prėskienis et al., 2021; Serikova et al., 2019). They typically contain large amounts of organic carbon leached from degrading permafrost soils (Tarnocai et al., 2009; Schuur et al., 2009), often leading to significant GHG emissions, along with pronounced seasonality in emission rates (Bouchard et al., 2015; Heslop et al., 2020; Kuhn et al., 2023; Matveev et al.,

Deleted: summer
Deleted: (0.7°C above the seasonal mean)
Formatted: Font: (Default) +Headings (Times New Roman)
Formatted: Font: (Default) +Headings (Times New Roman), Font color: Text 1
Formatted: Font: (Default) +Headings (Times New Roman), Not Bold, Font color: Text 1
Formatted: Font: (Default) +Headings (Times New Roman), Font color: Text 1
Formatted: Font: (Default) +Headings (Times New Roman), Font color: Text 1
Deleted: during a warmer one (2.6°C above the seasonal mean)
Formatted: Font color: Text 1
Deleted: peaked
Deleted: they
Deleted: were almost four times higher than those in summer

2016; Wik et al., 2016). Due to climate change and permafrost thawing, thermokarst lakes in some regions are still expanding downward and laterally, while others are experiencing drainage through changes in hydro-connectivity (Smith et al., 2005). As the ice-free season lengthens, warmer and wetter conditions may further enhance GHG production, originating either from thawing permafrost carbon or from freshly fixed carbon, each with distinct feedback effects (Prėskienis et al., 2021).

Much research to date has focused on large thermokarst lakes in areas of continuous permafrost with Yedoma soils (Pleistocene, ice-rich, carbon-rich permafrost). Thermokarst lakes in non-Yedoma landscapes of subarctic regions are typically small, shallow, and notably turbid (Grosse et al., 2013; Laurion et al., 2010; Bouchard et al., 2015; Crevecoeur et al., 2015; Wik et al., 2016). They result from the degradation of palsas (organic-rich mounds) or lithalsas (on mineral soils). Lakes on palsas tend to be dark and rich in organic matter, while those on lithalsas often display a range of colours resulting from the presence of suspended silts and clays, as well as varying amounts of organic matter leached from the watershed (Matveev et al., 2018). In subarctic areas, thousands of thermokarst lakes are smaller than 0.1 km^2 and often fall outside large-scale surface area classifications (Downing, 2010; Wik et al., 2016). Moreover, studies have reported increases in thermokarst lake area in recent decades, for example in Nunavik (northern Quebec), Canada, with a 96% increase from 1957 to 2009 (Jolivel and Allard, 2013). To better assess their contribution to the global carbon budget, both their areal extent and limnological functioning need to be evaluated.

GHG emissions from thermokarst lakes consist of diffusive and ebullitive fluxes. Diffusive emissions are influenced by gas accumulation in the upper layers of the water column and turbulence at the lake surface. Ebullitive fluxes, on the other hand, involve bubbles released from the sediments and depend on factors such as sediment temperature (Wik et al., 2014; Kuhn et al., 2021), atmospheric pressure (Goodrich et al., 2011), dominant vegetation and lake depth (Burke et al., 2019). Significant amounts of CH_4 are typically released through ebullition, with high release rates often observed in lakes with carbon-rich sediments, such as thermokarst lakes (Wang et al., 2021; Wik et al., 2016; Yang et al., 2023). Many studies have shown that ebullitive CH_4 fluxes are predominant in thermokarst lakes, largely overcoming diffusive fluxes (Walter et al., 2006; Sepulveda-Jauregui et al., 2015). However, other studies have reported cases where diffusive fluxes of CO_2 and CH_4 can dominate, potentially influenced by sediment type (Matveev et al., 2016; Matveev et al., 2018). N_2O emissions from thermokarst lakes are not well documented. N_2O concentrations reaching up to 222% saturation have been measured in the water column of a High Arctic thermokarst lake, highlighting the need for better quantification of N_2O emissions from these systems (Begin et al., 2021). However, studies have reported near-equilibrium N_2O concentrations in shallow northern lakes, including boreal (Huttunen et al., 2002), thermokarst (Abnizova et al., 2012), and eutrophic systems (Davidson et al., 2024).

In dimictic lakes, gases typically accumulate under the ice cover in winter and at the bottom of stratified lakes in summer, sometimes reaching concentrations that are orders of magnitude higher than at the surface. Therefore, spring and autumn are often marked by peaks in diffusive emissions as the water column mixes, a process known as the storage flux (Sepulveda-Jauregui et al., 2015; Greene et al., 2014). However, the mixing dynamics of thermokarst lakes differ from those of larger lakes due to their smaller fetch, partial wind sheltering, and higher concentrations of dissolved organic matter (DOM) and suspended solids. These factors can lead to distinct patterns of GHG outgassing accumulated over winter and summer,

Formatted: Subscript

especially during spring turnover, which may be brief or even absent in humic lakes (Matveev et al., 2019). Significant seasonal variations in diffusive emissions have been documented in thermokarst lakes across various regions (Hughes-Allen et al., 2021; Prėskienis et al., 2021; Zabelina et al., 2020).

Diel variations in diffusive emissions are also commonly observed in lakes during the open water period. While some studies report higher fluxes at night or in the early morning (Podgrajsek et al., 2014; Eugster et al., 2022; Zhao et al., 2024), others find increased emissions during the day (Sieczko et al., 2020; Martinez-Cruz et al., 2020; Erkkilä et al., 2018). It is generally accepted that diel wind patterns are closely linked to diel flux patterns in larger lakes, where nighttime is often characterised by low wind speeds and a stable atmospheric boundary layer. However, in smaller, sheltered systems, recent research suggests that nighttime diffusive fluxes may dominate (Walter Anthony and Macintyre, 2016). This is attributed to surface cooling, which generates large eddies that bring GHG-enriched water to the surface, as well as small eddies that enhance gas exchange at the water-air interface. Because thermokarst lakes typically contain high concentrations of chromophoric DOM (CDOM), they tend to be strongly stratified during summer, with a shallow, diurnal upper mixed layer. Thus, convection-enhanced diffusion may be a key driver of GHG emissions in these systems (Macintyre et al., 2010; Holgerson et al., 2016). Northern studies are often constrained by logistical challenges, with limited flux measurement points and a tendency to collect data only during the day–potentially introducing significant bias (Prėskienis et al., 2021; Hughes-Allen et al., 2021; Yang et al., 2023; Kuhn et al., 2023). Diffusive fluxes are commonly estimated using wind-driven models (Cole and Caraco, 1998; Wanninkhof, 2014), but these models are less accurate for very small, wind-sheltered lakes. While the eddy covariance method provides continuous measurements, it is less effective for small lakes due to footprint area constraints. Chamber-based methods, though more suitable, are limited to point measurements.

Upscaling emissions from small thermokarst lakes remains challenging due to their dynamic nature, variable morphology, and dependence on regional factors such as permafrost conditions, soil properties, and local meteorology. Simplified estimation methods can introduce substantial variability in results. Therefore, we highlight the need for more studies quantifying fluxes from these very small–but abundant–lakes, with careful consideration of diel and seasonal variability. Such efforts are essential for refining CO_2, CH_4, and N_2O flux estimates, which are key components of the global GHG budget.

This study quantified GHG emissions from two lithalsa thermokarst lakes in a subarctic region of Canada. Despite being located on the same degrading permafrost mound, the lakes differ in key characteristics: one is more sheltered and humic, while the other is wind-exposed and more transparent. The objectives were to (1) characterise their physicochemical properties, (2) assess the magnitude and diel variation of summer GHG fluxes, and (3) explore how seasonal patterns in limnophysical conditions may influence GHG dynamics. We conducted two contrasting summer campaigns in 2022 and 2023–one during a colder period and the other during a warmer one–focusing on temporal patterns in GHG diffusive fluxes and the magnitude of ebullitive fluxes in 2023. Additionally, we continuously monitored water column conditions for two years, alongside hourly meteorological data, enabling extrapolation beyond the flux observation period.

Formatted: Font: Not Bold, Font color: Text 1

Deleted: estimate seasonal variability.

2 Methods

2.1 Study site

The study site (56°33'28.8"N, 76°28'46.5"W) is located in the Tasiapik Valley, near the Inuit community of Umiujaq in Nunavik, Quebec, Canada. In the lower part of the valley, the surface deposits are predominantly marine silt, while the upper part consists of a thin layer of littoral sands. Discontinuous permafrost started penetrating the silt unit in the lower valley around 6500 years BP. In the upper valley, the sand layer generally prevented permafrost aggradation, but in areas with a thinner sand layer, the underlying silt froze, leading to the formation of permafrost mounds (Dagenais et al., 2020; Fortier et al., 2020).

The region has a subpolar continental climate, characterised by long winters and short, cool summers. Over the period 1997-2023, the mean annual air temperature was approximately –3°C. Vegetation in the Tasiapik Valley is highly variable: the upper valley is dominated by lichen-covered mounds surrounded by shrubs, while the lower valley is primarily covered by forested tundra. This diversity of vegetation types highlights the valley's role as an ecotone, a transitional zone between tundra and boreal forest ecosystems. Climate change trends observed in Nunavik indicate that permafrost in the region has been degrading over the past 25 years (Lemieux et al., 2016).

2.2 Lake surveys

We closely monitored two lakes located in the upper valley (Fig. 1), referred to as TAS1 and TAS3 for consistency with previously sampled lakes in the region (unpublished results). Two intensive summer campaigns were conducted: one from July 7-16, 2022, and another from August 9-21, 2023. Additionally, the lakes were continuously monitored from October 2021 to August 2023 to study their oxythermal structure. The two shallow thermokarst lakes are situated on a single degrading lithalsa mound, as shown in the bathymetric map (Fig. S1). Currently, they remain hydrologically isolated due to an underlying silt layer, with their interannual water balance entirely dependent on the ratio of annual precipitation to evaporation (Bussière et al., 2022). Given their shallow depth, water levels fluctuate significantly. In the future, these lakes may merge into a single waterbody. Like other lakes in the region, they are small, shallow, and strongly absorb light. Despite their size, they are stratified, with frequent anoxic conditions in bottom waters, similar to other subarctic thermokarst lakes (Matveev et al., 2018). TAS1 has a surface area of 186 m^2 (Table 1) and is located on the south side of the permafrost mound, surrounded by shrubs, though it remains relatively exposed to the wind (Fig. 1). In July 2022, its maximum water level was 2.60 ± 0.02 m, slightly decreasing to 2.50 ± 0.02 m in August 2023. Compared to TAS3, TAS1 has lower concentrations of dissolved organic carbon (DOC), CDOM absorption (at 320 nm, a_{320}), and total suspended solids (TSS), making it a more transparent lake with a Secchi depth (Z_{SD}) of 1.20 m. Nutrient concentrations were also high, with total phosphorus (TP) averaging 245 µg L^{-1} and total nitrogen (TN) 1337 µg L^{-1}, indicating high potential productivity (Table 2).

Deleted: 3

Deleted: very

Deleted:

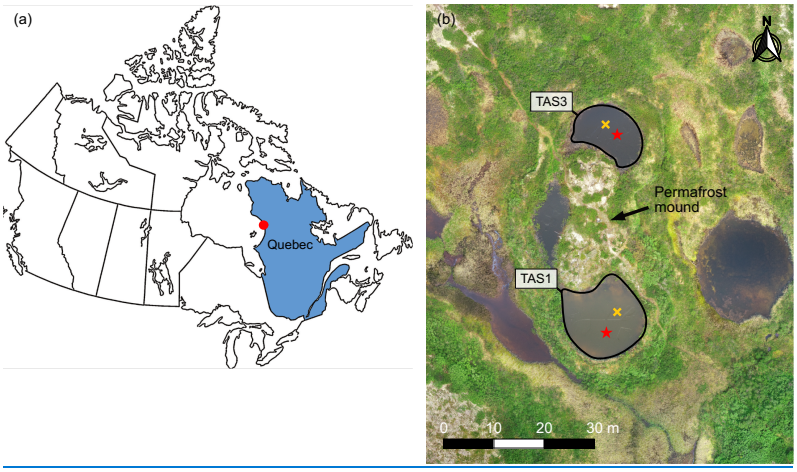

Figure 1. Location map of the Tasiapik Valley: (a) Map of Canada highlighting the study site marked with a red dot, and (b) areal contours of the two lakes under study. The mooring lines' locations are marked with red stars, while the bubble traps locations are marked with yellow crosses. Aerial photography by Madeleine St-Cyr.

Deleted:

TAS3 has a surface area of 131 m^2 and is located on the northern side of the permafrost mound (Table 1, Fig. 1). Surrounded by higher vegetated ramparts, it is shallower and more sheltered from the wind. The average water level fluctuated considerably between the two summer campaigns, reaching 1.80 ± 0.02 m in July 2022 and decreasing to 1.50 ± 0.04 m in August 2023. TAS3 is more humic than TAS1, with twice the DOC concentration and nearly three times the a_{320} values (Table 2). Its TSS level is also three times higher than in TAS1, making it more opaque, with a Z_{SD} of just 55 cm. Despite these differences, TAS3 exhibited similarly high nutrient concentrations to TAS1 (Table 2).

Table 1. Morphometric characteristics of the studied thermokarst lakes, derived from bathymetric maps created in July 2022, along with Secchi depth measurements.

Lake	Area (m^2)	Wind exposure	Max. depth (m)	Mean depth (m)	Secchi depth (m)
TAS1	186	exposed	2.5	1.2	1.20
TAS3	131	sheltered	1.9	0.7	0.55

Deleted: 3

Deleted: 6

Table 2. Chemical and optical properties of the two lakes surveyed in 2022 and 2023, including the absorption coefficient at 320 nm (a_{320}; a proxy for chromophoric dissolved organic matter), dissolved organic carbon (DOC), specific ultraviolet absorbance at 254 nm ($SUVA_{254}$), total nitrogen (TN), total phosphorus (TP), pH, conductivity, and total suspended solids (TSS). Data are presented for both surface and bottom samples. na = not available.

Lake	Depth	a_{320} (m^{-1})	DOC (mg L^{-1})	$SUVA_{254}$ (L mg^{-1} m^{-1})	TP (µg L^{-1})	TN (µg L^{-1})	pH	Conductivity (µS cm^{-1})	TSS (mg L^{-1})
July 2022									
TAS1	surface	8.4	4.4	2.0	48	439	7.8	24.0	7.0
	bottom	3.7	2.5	1.6	350	1886	6.4	40.0	na
TAS3	surface	28.1	7.4	3.8	109	804	6.5	20.0	22.0
	bottom	30.4	7.1	4.0	132	920	6.1	21.0	26.0
August 2023									
TAS1	surface	11.6	8.6	1.5	111	884	6.6	24.8	16.0
	bottom	3.1	4.9	0.8	472	2139	6.1	117.0	118.0
TAS3	surface	38.7	10.5	3.6	159	1444	na	17.6	6.0
	bottom	40.6	7.1	5.2	446	2242	5.6	46.0	40.0

2.3 Meteorological conditions

To relate oxythermal conditions and GHG fluxes from the lakes to atmospheric conditions, air temperature, wind speed, and wind direction were obtained from a meteorological station located 200 m from the main site (Cen, 2024). In addition, local wind speed was measured 0.2 m above the water surface of both lakes during the intensive summer campaigns using DS-2 Sonic Anemometer (resolution: 0.01 m s^{-1}, 1°) mounted on a small floating platform. To estimate the roughness length (z_0), we applied the logarithmic wind profile equation using the wind speed measurements taken at 0.2 m above the lakes during the two intensive campaign periods, along with wind speed data from the nearby meteorological station at 10 m height. Calculations were performed under quasi-neutral atmospheric conditions (bulk Richardson number between –0.05 and +0.05), yielding z_0 values of 0.087 m at TAS1 and 0.112 m at TAS3.

2.4 Limnological profiling

The oxythermal structure was continuously monitored from 7 July 2022 to 21 August 2023 for TAS1 and from 28 September 2021 to 21 August 2023 for TAS3. Dissolved oxygen (PME miniDOT, ±10 µM, ±0.1°C), conductivity (HOBO U24-001, ±1 µS cm^{-1}, ±0.1°C), and pressure (HOBO U20L-01, ±0.3% FS, ±0.44°C) were recorded at the surface and bottom only. As these loggers also recorded temperature, water temperature was measured at a total of six depths, including four additional depths with HOBO U22-001 (±0.21°C) (see logger depths in Table S1). The submersible automated data loggers were installed on a mooring line at the deepest point of each lake and recorded at hourly intervals (Fig. 2). The buoy was positioned just below the water level to avoid interference from ice during the winter. As the water level was lower in August 2023, the buoy was slightly above the surface, bringing the loggers closer to the surface than in July 2022.

In addition to continuous data collected by the loggers, manual measurements of temperature, dissolved oxygen, and conductivity were conducted. In 2022, data were recorded using a portable YSI ProODO device (resolution: 0.1% for dissolved oxygen, 0.1°C for temperature) and a Seven2Go™ conductivity meter (resolution: 0.01 µS cm^{-1}). In 2023, measurements were taken with a ProSOLO device (resolution: 0.1% for dissolved oxygen, 0.1°C for temperature, 0.001 mS cm^{-1} for conductivity). The buoyancy frequency (N, cycles per hour), which quantifies water column stability, was calculated using the following equation:

$$N = \sqrt{-\frac{g}{\rho}\frac{d\rho}{dz}}\frac{3600}{2\pi} \quad (1)$$

where g is the acceleration due to gravity (9.81 m s^{-2}), ρ is the water density (kg m^{-3}), and z is the depth (m). Water density was derived from our in-situ measurements of temperature at surface and bottom of each lake using Kell equation (Jones and Harris, 1992). This allowed us to estimate the vertical density gradient ($d\rho/dz$). To quantify the stabilizing effect of stratification relative to the destabilizing effect of wind-induced shear, the Wedderburn number (W) was calculated as:

$$W = \frac{g}{\rho}\frac{\Delta\rho\, h^2}{u_{*w}^2\, L} \quad (2)$$

where $\Delta\rho$ is the density difference across the diurnal thermocline (kg m^{-3}), h is the depth of the thermocline (m), ρ is the average water density (kg m^{-3}), u_{*w} is the friction velocity (m s^{-1}), and L is the length of the lake in the wind direction (m). Values of $W > 10$ indicate minimal thermocline tilting, $1 < W < 10$ indicate partial tilting, and $W < 1$ indicate full upwelling.

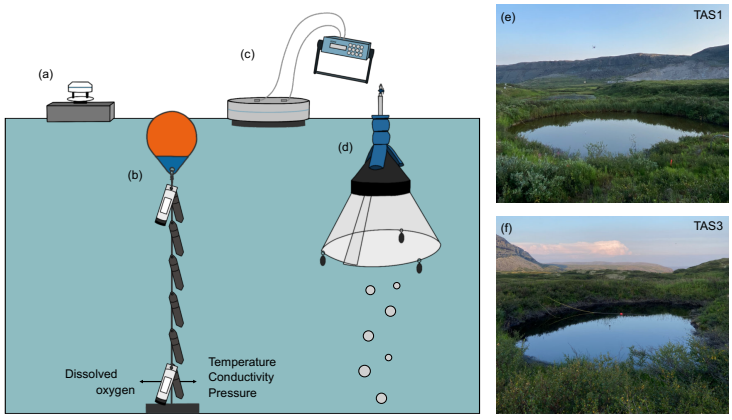

Figure 2. Schematic of the instrumentation deployed in the lakes, including: (a) an anemometer mounted on a floating platform (deployed in July 2022 and August 2023), (b) a mooring line equipped with data loggers for continuous oxythermal measurements, (c) a floating chamber connected to an infrared CO_2 analyzer (deployed in July 2022 and August 2023), and (d) a bubble trap (deployed in August 2023). Panels (e) and (f) show photographs of TAS1 and TAS3, respectively.

Deleted: where g is the acceleration due to gravity (9.81 m s^{-2}), ρ is the water density (kg m^{-3}), and z is the depth (m).

Formatted: Font: (Default) Times New Roman, 10 pt, Font color: Text 1

Formatted: Font: (Default) Times New Roman, 10 pt, Font color: Text 1

Formatted: Font: 10 pt, Font color: Text 1

Formatted: Font: (Default) Times New Roman, 10 pt, Font color: Text 1

Formatted: Font: 10 pt, Font color: Text 1

Formatted: Font: (Default) Times New Roman, 10 pt, Font color: Text 1

Formatted: Font: 10 pt, Font color: Text 1

Formatted: Font: (Default) Times New Roman, 10 pt, Font color: Text 1

Formatted: No Spacing, Justified, Space After: 6 pt, Line spacing: 1.5 lines

Formatted: Font: (Default) Times New Roman, 10 pt

2.5 Water chemistry

Several limnological characteristics were measured in each lake during the intensive campaigns, including TP, TN, TSS, pH, conductivity, DOC, and CDOM. TP and TN were quantified from unfiltered water samples collected in 50 mL plastic tubes, which were acidified with H_2SO_4 to a pH of 2 and stored at 4°C until analysis by colorimetry following digestion (details in Bartosiewicz et al. (2016)). For CDOM and DOC, water samples were filtered through pre-rinsed polyethersulfone (PES) filters (0.2 µm porosity) and stored in amber glass vials at 4°C. For DOC analysis, 40 µL of pure HCl was added to the vials to adjust the pH to 2 prior to analysis using a Total Organic Carbon analyzer (Aurora 1030W, O.I. Analytical) with the persulfate oxidation method. CDOM samples were brought to room temperature within a week of field collection, and absorbance scans were conducted between 200 and 800 nm using a dual beam spectrophotometer (Varian Cary 100 Bio UV-Visible, ± 2 nm) with a 1-cm pathlength quartz cuvette. Null-point adjustment was applied to blank-corrected absorbance spectra using the mean value from 790 to 800 nm. The absorption coefficient at 320 nm (a_{320}) was used as a proxy for CDOM concentration. For TSS, water samples were filtered onto pre-burned and pre-weighed glass fiber filters (GF75, 0.7 µm nominal porosity, Advantec). The filters were stored in aluminum foil in the freezer and then dried overnight at 60°C to determine TSS content.

2.6 GHG flux measurements and estimations

To estimate GHG fluxes, we measured the dissolved concentrations of CO_2, CH_4, and N_2O, as well as CO_2 diffusive fluxes using a floating chamber during the intensive summer campaigns in July 2022 and August 2023. At each lake, measurements were taken over multiple consecutive days across different hours of the day and night. This approach allowed us to reconstruct diel variability in gas fluxes, dissolved gas concentrations, and k_{600}, providing between 9 and 13 data points per lakes for both intensive campaigns. Ebullitive fluxes of CO_2 and CH_4 were measured at the center using an inverted funnel submerged below the water surface. CO_2-equivalent emissions were calculated by applying a global warming potential (GWP) values of 27 for CH_4 and 273 for N_2O, based on a 100-year time horizon, with CO_2 having a GWP value of 1 (IPCC, 2023). All data are presented in Eastern Standard Time (EST).

Deleted: .

Formatted: Font: Not Bold, Font color: Text 1

2.6.1 Dissolved gas concentrations

Dissolved gas concentrations were obtained at the lake surface during each diffusive flux measurement using the headspace method. To account for the accumulation of GHG in the water column, gases were also collected at various depths. In 2022, four profiles were carried out (10, 80, 160, and ~230 cm at TAS1; 10, 50, ~105, and ~155 cm at TAS3). In 2023, two profiles were conducted (10, 120, and 230 cm at TAS1; 10, 70, and 140 cm at TAS3). Water samples were collected from the centre of the lakes using a Van Dorn horizontal sampler (integrating a depth layer of ~15 cm). The water was immediately transferred to a 2 L LDPE gas exchange bottle, except at the surface, where it was sampled directly into the bottle. A 30 mL headspace of atmospheric air was created using a syringe connected to an inlet at the bottom of the bottle. The bottle was shaken vigorously

for 3 min, and 20 mL of the gaseous headspace was transferred to a 12 mL gas-tight Exetainer vial that had been pre-flushed twice for 10-15 seconds with nitrogen and vacuumed twice for 3 minutes. Water temperature was measured at the beginning and end of the exchange process. Atmospheric samples were also taken daily. Gas samples were analysed using a Trace 1310 gas chromatograph (Thermo Fisher Scientific). We used two parallel channels, one with TCD-FID detectors (column HSQ 80/100, MS 5A 80/100) for CH_4 and CO_2, and one with an ECD detector (column HSQ 80/100) for N_2O. Calibration curves were established for CO_2 (up to 10 000 ppm), CH_4 (up to 45 000 ppm), and N_2O (up to 1 ppm). Detection limits were 200 ppm for CO_2, 3 ppm for low CH_4 concentrations, 50 ppm for CH_4 concentrations above 1000 ppm, and 0.1 ppm for N_2O. Dissolved CH_4 and CO_2 concentrations were calculated using Henry's Law, adjusted for temperature and atmospheric pressure.

Formatted: Font color: Auto
Deleted: with nitrogen
Deleted: and vacuumed.
Formatted: Font: (Default) Times New Roman, Not Bold, Font color: Auto
Formatted: Font color: Auto
Deleted: ; column capacity 4, TCD detector
Formatted: Font: (Default) Times New Roman, Not Bold, Font color: Text 1
Formatted: Font:

2.6.2 Diffusive fluxes

Diffusive fluxes (F_D) of CO_2 (mmol m^{-2} d^{-1}) were measured over a full diel cycle during both intensive campaigns (18 measurements in 2022 and 24 in 2023; see Table S2). These fluxes were obtained by monitoring gas concentration in a floating chamber (area: 0.147 m^2, volume: 0.0128 m^3, including volume of the tube) connected to an infrared gas analyser (EGM4, PP Systems) for approximately 30 min, following the method of Macintyre et al. (2021):

Deleted:)

$$F_D = \frac{S\,P\,V_{ch}}{R\,T\,A_{ch}}\,D \quad (3)$$

where S is the linear slope of CO_2 (ppm) versus time, P is the atmospheric pressure (Pa), V_{ch} is the chamber volume (m^3), R is the gas constant (J mol^{-1} K^{-1}), T is the water temperature (K), A_{ch} is the chamber surface area (m^2), and D is a unit conversion factor to obtain flux values in mmol m^{-2} d^{-1}.

To estimate the CH_4 and N_2O fluxes, we used the concentration gradient and the gas transfer velocity (k):

$$F_D = k\left(C_{sf} - C_{eq}\right) \quad (4)$$

where C_{sf} is the gas concentration at the water surface (obtained from the headspace method), and C_{eq} the aqueous gas concentration in equilibrium with the atmosphere at ambient temperature, both in µM. From this equation, we obtained the k value for CO_2 using direct flux measurements from the chamber and surface water CO_2 concentrations. The corresponding k values for CH_4 and N_2O were computed using the following equation:

$$k_x = k_{CO_2}\left(\frac{Sc_x}{Sc_{CO_2}}\right)^{-n} \quad (5)$$

where Sc_x is the Schmidt number (the ratio of kinematic viscosity and molecular diffusion) for gas x at ambient temperature. The exponent n was set to 1/2 when wind speeds exceeded 3.6 m s^{-1}, and 2/3 when wind speeds were below 3.6 m s^{-1} (Jähne et al., 1987).

2.6.3 Ebullitive fluxes

Ebullitive fluxes (F_E) of CO_2 and CH_4 were measured in 2023 following the method outlined by Wik et al. (2013). Bubble traps, consisting of inverted funnels with a collection area of 0.23 m^2, were installed for a total 11 days in both lakes (Fig. 2). The traps were anchored with submerged weights and tied with ropes to fixed shoreline points to minimize movement and drifting. They were positioned near the lake center to improve representativity of ebullition across the central lake area. N_2O concentrations could not be quantified due to interference from high CH_4 concentrations. The bubble traps were connected to a 140 mL graduated polypropylene syringe and were sampled every 1 to 4 days, depending on the gas accumulation rate. Gas was collected in two replicates (Exetainers) for quantification by gas chromatography. Ebullitive fluxes (F_E) were calculated using the following equation:

$$F_E = \frac{P\,V_g}{\Delta t\,V_m\,A} \quad (6)$$

where P is the partial pressure of the gas (dimensionless), V_g is the total volume of gas in the funnel (m^3), Δt is the time interval between two measurements (days), V_m is the molar volume of gas at local air temperature ($m^3\ mol^{-1}$), and A is the collection area of the funnel (m^2).

3 Results

We first present the annual variations in temperature, oxygen, and conductivity observed in the two thermokarst lakes. We then detail the results from the two intensive campaigns, including meteorological conditions, physicochemical profiles, and GHG concentrations and fluxes, to examine the magnitude and diel variations during the summer.

3.1 Seasonal profiles

Both lakes had an open-water period of approximately five months (June to October) and remained ice-covered for about seven months (November to May) (Fig. 3). Ice cover duration was determined using Sentinel-2 imagery analysis with an ice detection algorithm through the Google Earth Engine platform, following the approach of Domart et al. (2024). In the winter preceding the 2022 summer campaign, ice began forming on both lakes on 10 November 2021, with ice breakup occurring on 6 June 2022 for TAS1 and 3 June 2022 for TAS3. In the following winter, ice cover formed on both lakes from 10 November 2022 and lasted until 6 June 2023 for TAS1, whereas TAS3 experienced earlier ice breakup on 19 May 2023. During summer, both lakes underwent partial mixing events due to their sensitivity to temperature fluctuations, which caused stratification to weaken rapidly, making the lakes more susceptible to wind-driven mixing. However, complete mixing only occurred in autumn and spring, classifying them as dimictic lakes, although the spring mixing period was notably brief.

Deleted: 2.7 Larger scale estimates¶
To estimate annual GHG diffusive emissions from the lakes, we calculated the average, minimum, and maximum fluxes for summer 2022, fall 2022, spring 2023, and summer 2023. For each season, Equation 4 was applied using the minimum and maximum concentration gradients estimated for that season, along with the average gas transfer velocity (k) over the corresponding period. We estimated k_{600}, the gas transfer velocity normalized to a Schmidt number of 600, to calculate k with equation 5. Limnological seasons were defined based on changes in the thermal structure of the water column. For summer comparisons, the period from 7 July to 20 August was used, as data were available for both 2022 and 2023. Fall 2022 and spring 2023 were defined as the periods from September to October and mid-May to mid-June, respectively. ¶
To estimate the concentration gradients for each season, differ… [1]

Deleted: Finally, we provide broader estimates comparing GHG fluxes across summer, fall, and spring.

Deleted: have …ad an open-water period of approximately five months (June to October) and remained ice-covered for about seven months (November to May) (Fig. 3). Ice cover duration was determined using Sentinel-2 imagery analysis with an ice detection algorithm through the Google Earth Engine platform, following the approach of Domart et al. (2024). In the winter preceding the 2022 summer campaign, ice began forming on both lakes on 10 November 2021, with ice breakup occurring on 6 June 2022 for TAS1 and 3 June 2022 for TAS3. In the following winter, ice cover lasted formed on both lakes from 10 November 2022 and lasted until to…6 to…6 June 2023 for TAS1, whereas TAS3 experienced earlier ice breakup on 19 May 2023. During summer, both lakes underwentgo…partial mixing events due to their sensitivity to temperature fluctuations, causing …hich caused stratification to weaken rapidly, and …aking them …he lakes more susceptib… [2]

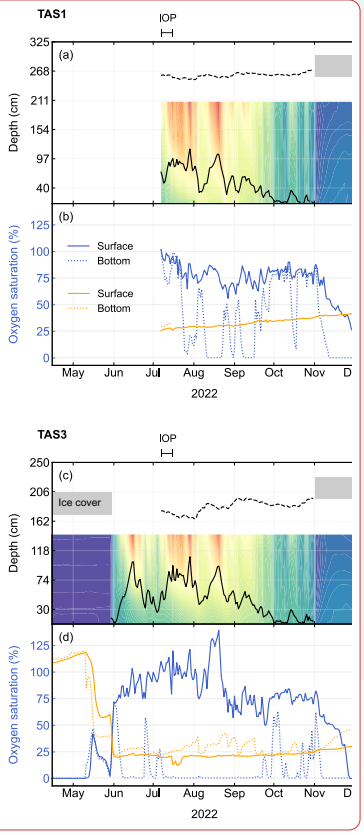

Deleted:

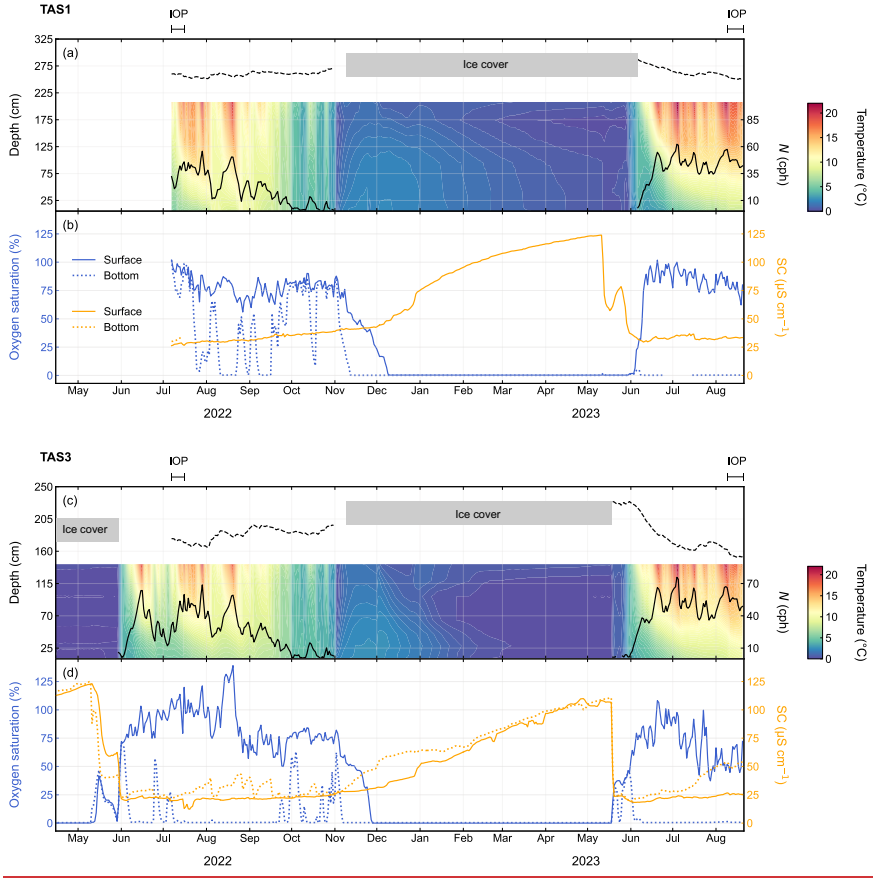

Figure 3. Physicochemical profiles from summer 2022 to summer 2023, showing temperature and buoyancy frequency *N* for (a) TAS1 and (c) TAS3, with the water surface marked by a black dotted line. Oxygen saturation and specific conductivity (SC) are shown for (b) TAS1 and (d) TAS3. Temperature at the very surface was not measured, as the buoy was positioned below the air-water interface to prevent it from becoming trapped in the ice cover. Nevertheless, winter temperature data suggest that ice may have grown over the buoys, pushing down the mooring and changing the depth of surface sensors, making surface data unreliable. Intensive summer campaign periods are indicated by brackets for July 2022 and August 2023.

Deleted:

At TAS1, the mooring was installed from 7 July 2022 to 21 August 2023, so data from the spring mixing period and the onset of stratification before the 2022 summer campaign are unavailable. However, air temperature data indicate a colder period between late June and early July 2022 (Fig. S2). This likely led to full oxygenation of the bottom waters by mid-July, as shown by the bottom oxygen logger positioned at 58 cm above the lake bottom (logger depths in Table S1). During the 2022 summer, alternating phases of partial mixing and stratification were observed (Fig. 3a). After a brief period of stratification at the end of July, marked by a peak N value of 64 cph (black curve in Fig. 3a), weakened stratification followed from 4 to 11 August with an N value of 7.5 cph, then stronger stratification by 23 August with N reaching 57.1 cph. Stratification weakened at the end of August, with autumnal mixing beginning by mid-September 2022, followed by reverse stratification from 2 November. Bottom waters turned fully anoxic by 12 November, while surface anoxia was not detected until 9 December. Ion accumulation under the ice throughout the winter increased conductivity to a maximum of 124 µS cm^{-1} before it dropped on 12 May 2023, likely due to partial ice melt before full ice-off by 6 June 2023. Temperature, conductivity, and oxygen profiles suggest that the spring mixing period in TAS1 was extremely brief, lasting only about five days (1-5 June 2023, Fig. 3a,b), but oxygen levels remained near anoxia. Surface oxygen began to increase on 5 June, yet bottom anoxia returned as early as 8 June. Throughout the summer of 2023, thermal stratification persisted, being more pronounced than in 2022 and maintaining bottom anoxia. During the comparable summer period (7 July-21 August), the average N value was 44.6 cph in 2023, compared to 34.4 cph in 2022. Oxygen data from 26 June to 14 July 2023 were deemed unreliable for TAS1 and had to be discarded. However, the thermal structure suggests that anoxic conditions likely persisted during this period (indicated by the red dotted line in Fig. 3b).

At TAS3, the mooring was deployed for nearly two years, from 28 September 2021 to 21 August 2023. During the first recorded winter in 2022, ion accumulation under the ice increased conductivity to a maximum of 123 µS cm^{-1} before it dropped on 11 May 2022, likely due to partial ice melt. The spring mixing period lasted approximately 23 days (11 May-3 June; Fig. 3c,d), as indicated by conductivity and oxygen data. Thermal stratification established quickly, leading to rapid bottom-water deoxygenation, with complete anoxia occurring within five days (Fig. 3c,d), as recorded by the oxygen logger positioned at 44 cm above the sediment layer (Table S1). From 25 June to 10 July, cooler weather allowed brief reoxygenation events to occur (e.g. on 25 June and 4 July; N = 7.5 cph). This was followed by alternating stratification and mixing, with N reaching a maximum of 80.4 cph by late July and a minimum of 17.3 cph at the beginning of August. Strong stratification re-established itself in mid-August, with N reaching 61.6 cph, and intermittent weakening occurred thereafter. Yet bottom waters remained anoxic until the autumn turnover, which started in mid-September. However, bottom-water reoxygenation remained incomplete prior to ice formation. As observed at TAS1, inverse stratification set in on 2 November, leading to full bottom-water anoxia by 7 November, which progressively reached the surface by 27 November. Winter conductivity peaked at 110 µS cm^{-1} before it dropped on 19 May 2023 following ice breakup. Spring turnover was shorter than in spring 2022 (~13 days, 19 May-1 June 2023, Fig. 3c,d), and stratification redeveloped more quickly, leading to near-instantaneous bottom anoxia by 9 June 2023. As for TAS1, thermal stratification persisted throughout summer in 2023 and was stronger than in 2022 (average

Formatted: Font color: Auto
Deleted: , with an average daily air temperature of 6.2°C from 23 June and 11 July
Formatted: Font color: Auto
Deleted:
Deleted: 2022
Deleted: cycles per hour…ph (cph; … [3]
Deleted: partial mixing and
Deleted: a colder spell
Formatted: Font color: Auto
Formatted: Font color: Auto
Deleted: 2022
Deleted: weakened stratification, causing
Deleted: to drop
Deleted: to a minimum of ….5 cph, then … [4]
Deleted: and resulting in partial mixing of the water colum … [5]
Deleted: was then re-established, reaching a maximum
Deleted: *N* of
Formatted: Font color: Auto
Formatted: Font: Italic
Deleted: on 23 August, before another partial mixing event led to a decline in *N* to 6.5 cph until 8 September
Deleted: Stratification weakened at the end of August and … [6]
Deleted: . F…ull ice-off occurred …y 6 June 2023. Temper … [7]
Deleted: ,
Deleted: window
Deleted: … … [8]
Formatted: Font color: Auto
Formatted: Font color: Auto
Deleted:
Deleted: ¶ … [9]
¶
¶
¶ … [10]
Formatted … [11]
¶ … [12]
¶ … [13]
Formatted: Font: Times New Roman, 10 pt
¶
¶ … [14]

N during 7 July-21 August is 50.8 cph *vs.* 41.2 cph). From 8 July 2023 onward, bottom-water conductivity progressively increased, likely due to the stronger and more persistent stratification in this warmer year.

3.2 Meteorological conditions

Overall, summer 2022 was colder than summer 2023, with an average air temperature of 10.3 ± 4.7°C for mid-June to August 2022 compared to 13.6 ± 4.3°C in 2023, diverging from seasonal normal by –0.9 °C and +2.4 °C, respectively. Because the intensive campaigns were conducted in different months (July 2022 and August 2023), meteorological comparisons focus on those specific periods.

Weather conditions varied considerably between the two intensive campaign periods, with July 2022 being significantly colder and windier than August 2023. The mean air temperature during the July 2022 campaign was 8.8 °C (range: 1.3-23.1 °C), which is –2.7 °C below July normal (11.5 ± 5.1 °C). Whereas in August 2023, it was substantially warmer at 14.6 °C (range: 6.6-23.4 °C), which is +2.8 °C above August normal (11.8 ± 4.1 °C). The mean wind speed at 10 m height was 4.0 ± 1.7 m s^{-1} in July 2022, compared to 3.5 ± 2.0 m s^{-1} in August 2023. Closer to the water surface (0.2 m above), wind speeds were on average 1.4 times higher in 2022 than in 2023. Wind conditions also varied between the sampling sites, with TAS1 experiencing wind speeds 1.5 times higher than TAS3 on average (Fig. 4), as TAS3 is more sheltered by surrounding vegetation and topography. In both years, prevailing surface winds of TAS1 were mainly from the north and west, whereas winds at TAS3 predominantly came from the west (Fig. S3).

Formatted: Font: Italic, Font color: Auto
Formatted: Font color: Auto
Deleted: ¶
Deleted: 1
Deleted: 5
Deleted: 0
Deleted: , July and
Deleted: (0.7°C above seasonal normal)
Deleted: 1
Deleted: 4
Deleted: (2.6°C above seasonal normal)
Deleted: Since the intensive campaigns took place at different periods in each summer, meteorological comparisons are made between July 2022 and August 2023.
Formatted: Font: Times New Roman, 10 pt, Font color: Text 1
Deleted:

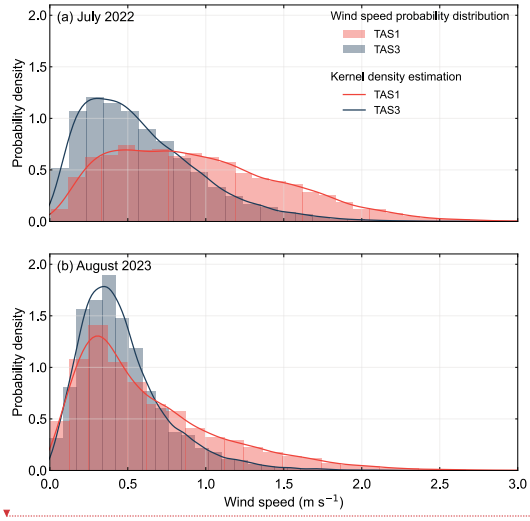

Figure 4. Wind speed probability density function and kernel density estimation at the surface (0.2 m from surface) of TAS1 and TAS3 during the intensive summer campaigns of (a) 7-16 July 2022 and (b) 9-21 August 2023.

3.3 Vertical structure of the water column during the intensive sampling periods

Vertical profiles collected manually from the lakes are presented on Figure 5. Temperature profiles (Fig. 5a,d) indicate that stratification was most pronounced in August 2023, due to warmer conditions and the later timing within the open water season (by one month). Despite their shallow depths (2.5-2.6 m at TAS1 and 1.5-1.8 m at TAS3), both lakes exhibited oxygen stratification, with anoxic conditions at the bottom during both observation periods (Fig. 5b,e).

Prior to the 2022 intensive campaign, the lakes had recently undergone a 15-day partial mixing event (25 June-10 July), as indicated by the weaker stratification and bottom-layer reoxygenation at TAS3 (Fig. 3c,d). This mixing event likely released accumulated gases from the previous winter and stratification period. During this time, mixed surface layers were significantly deeper than in August 2023. Based on the rapid decline in dissolved oxygen marking the boundary of the isolated layer, mixed layers extended to 2.1 m at TAS1 and 1.1 m at TAS3 (Fig. 5). These deeper mixed layers allowed a larger portion of the water column to interact with the atmosphere, resulting in greater oxygenation, with levels nearing 100% saturation (Fig. 5). In TAS3, oxygen supersaturation was observed on the afternoon of 6 July, reaching up to 124% near the surface and extending down to 0.9 m. However, below the mixed layer, oxygen remained depleted, suggesting the accumulation of GHGs. Despite

Deleted: ¶ ... [15]

Deleted: Weather conditions varied considerably between these two sampling periods, with July 2022 being significantly colder and windier than August 2023. The mean air temperature during the July 2022 campaign was 8.8°C (range: 1.3-23.1°C), whereas in August 2023, it was substantially warmer at 14.6°C (range: 6.6-23.4°C). The mean wind speed at 10 m height was 4.0 ± 1.7 m s^{-1} in 2022, compared to 3.5 ± 2.0 m s^{-1} in 2023. Closer to the water surface (0.2 m above), wind speeds were on average 1.4 times higher in 2022 than in 2023. Wind conditions also varied between the sampling sites, with TAS1 experiencing wind speeds 1.5 times higher than TAS3 on average (Fig. 4), as TAS3 is more sheltered by surrounding vegetation and topography. In both years, prevailing surface winds of TAS1 were mainly from the north and west, whereas winds at TAS3 predominantly came from the west (Fig. S3).¶

Deleted: Both lakes exhibited thermal stratification during the two intensive observation periods (indicated by brackets in Fig. 3).

Deleted: presents individual vertical profiles collected manually from the lakes

Deleted:

Deleted:

Deleted: .

the small fetch of these lakes (~15 m at TAS1 and ~12 m at TAS3), our estimations revealed low Wedderburn numbers (W) during the day (Fig. S4), indicating susceptibility to mixing as wind increased. At TAS3, W mostly indicated partial thermocline tilting ($1 < W < 10$) during the day, whereas at TAS1, it generally suggested minimal tilting (> 10). By mid-July (from 12 July), as temperature warmed and wind was weaker, values suggested minimal thermocline tilting in both lakes.

In contrast, during the August 2023 campaign, strong thermal stratification prevailed, leading to anoxic bottom waters from early June in both lakes. The mixed layers were much shallower–only 1.0 m at TAS1 and 0.5 m at TAS3. This stronger thermal stratification was reflected in the sharper oxygen concentration gradient, especially at TAS3, and a larger part of the water column that remained anoxic. Additionally, the specific conductivity increased considerably with depth, particularly at TAS1 (up to 128 µS cm^{-1} or total dissolved solids of 123 mg L^{-1}), which contributed to stronger density stratification. For example, temperature accounted for a density difference of 1.796 kg m^3 on 13 August while conductivity contributed approximately to 0.074 kg m^3, based on the simplified relationship of $\rho = 1000 + TSD \times 0.695 \times 10^{-3}$ kg m^3 (Collins, 1987). Our estimations of W mostly indicated partial tilting during the day but minimal tilting at night (reaching up to 10^8 on 15 August). Episodes of full upwelling ($W < 1$) were estimated during the day on 11 and 17 August TAS3. Throughout both intensive campaigns, TAS3 consistently showed lower W values, suggesting a greater potential for tilting compared to TAS1.

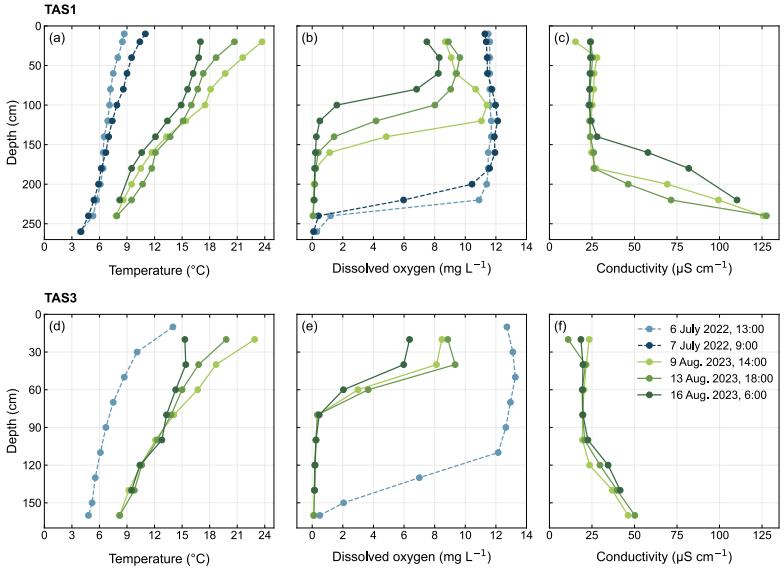

Figure 5. Vertical profiles of temperature, dissolved oxygen and specific conductivity in TAS1 (top panels) and TAS3 (bottom panels). Dotted lines are profiles in 2022, and solid lines are profiles in 2023.

Formatted: Font: Font color: Auto

Formatted: Font: Font color: Text 1

Deleted: Greater light attenuation was also observed at TAS3, where a_{320} values were more than three times higher than at TAS1 in both years (Table 2). Additionally, specific conductivity at the bottom showed considerable differences in 2023. While surface remained similar, conductivity increased with depth, especially at TAS1 (up to 128 µS cm^{-1}), contributing to stronger density stratification

Formatted: Font: Font color: Text 1

Formatted: Font color: Auto

Formatted: Font: Times New Roman, 10 pt, Font color: Auto

Formatted: Font color: Auto

Formatted: Font color: Auto

Formatted: Font color: Auto, Superscript

Formatted: Font color: Auto

Formatted: Font: Times New Roman, 10 pt, Font color: Auto

Formatted: Font color: Auto

Formatted: Font color: Auto

Formatted: Font color: Auto, Superscript

Formatted: Font color: Auto

Formatted: Font: Times New Roman, 10 pt, Font color: Auto

Formatted: Default Paragraph Font, Font: Times New Roman, 10 pt, Font color: Auto

Formatted: Default Paragraph Font, Font: Italic, Font color: Auto

Formatted: Default Paragraph Font, Font color: Auto

Formatted: Default Paragraph Font, Font color: Auto

Formatted: Default Paragraph Font, Font color: Auto

Formatted: Not Superscript/ Subscript

Formatted: Font: Times New Roman, 10 pt, Font color: Auto

Deleted: ¶

Despite the small fetch of these lakes (~15 m at TAS1 and ~12 m at TAS3), our estimations revealed low Wedderburn numbers (W) during the day in both intensive campaigns (Fig. S4), indicating susceptibility to mixing as wind increased. During the 2022 intensive campaign, W mostly indicated partial tilting ($1 < W < 10$) during the day at TAS3, whereas at TAS1, they generally suggested minimal tilting (> 10). By mid-July (from 12 July), values suggested minimal tilting in both lakes, particularly at night. In August 2023,

Deleted: ¶

3.4 Summer GHG concentrations

During both intensive summer campaigns, the lakes were supersaturated with CO_2 and CH_4 at the bottom but mostly undersaturated with N_2O (Fig. 6). In the July 2022 campaign, increased accumulation of GHGs in the bottom layers resulted in a pronounced vertical gradient of gas concentrations. Specifically, CO_2 concentrations at the bottom were, on average, 11 times higher than at the surface, while the CH_4 gradient was even more pronounced, with bottom concentrations 144 times greater than at the surface on average. In contrast, N_2O concentrations decreased with depth, with surface values on average 1.2 times lower than those in the deeper layers. These gradients resulted in surface gas concentrations that were mostly above air equilibrium for CO_2, CH_4 and N_2O (Table 3, Table S4). To assess gas saturation, we used global atmospheric partial pressure values, which averaged 20.1 µM for CO_2, 0.0034 µM for CH_4, and 12.0 nM for N_2O (grey section, Fig. 6). Moreover, differences in surface dissolved gas concentrations were observed between the two lakes. CO_2 and CH_4 surface concentrations were respectively 1.5 and 2.9 times higher at TAS1 compared to TAS3, despite similar bottom concentrations of both gases and a lower pH at TAS3, which could have favored CO_2 solubility (Table S5, Table 2).

Deleted: 3

Table 3. Near-surface CO_2, CH_4 and N_2O concentrations measured at TAS1 and TAS3. Values are presented as mean ± standard deviation (min-max). *N* =10 for 2022 and *N* =13 for 2023.

	Surface CO_2 (µM)		Surface CH_4 (µM)		Surface N_2O (nM)	
Period	TAS1	TAS3	TAS1	TAS3	TAS1	TAS3
July 2022	37.0 ± 5.5 (27.0 - 43.3)	25.0 ± 7.5 (10.2 - 34.3)	1.3 ± 0.4 (0.9 - 2.3)	0.4 ± 0.1 (0.3 - 0.6)	13.9 ± 0.9 (12.5 - 15.2)	13.5 ± 1.1 (11.9 - 14.9)
August 2023	51.1 ± 32.6 (21.4 - 122.5)	94.2 ± 75.0 (28.5 - 236.2)	1.8 ± 0.7 (1.1 - 3.2)	3.5 ± 2.4 (1.1 - 9.9)	4.0 ± 0.4 (3.3 - 4.6)	3.3 ± 0.3 (2.7 - 3.7)

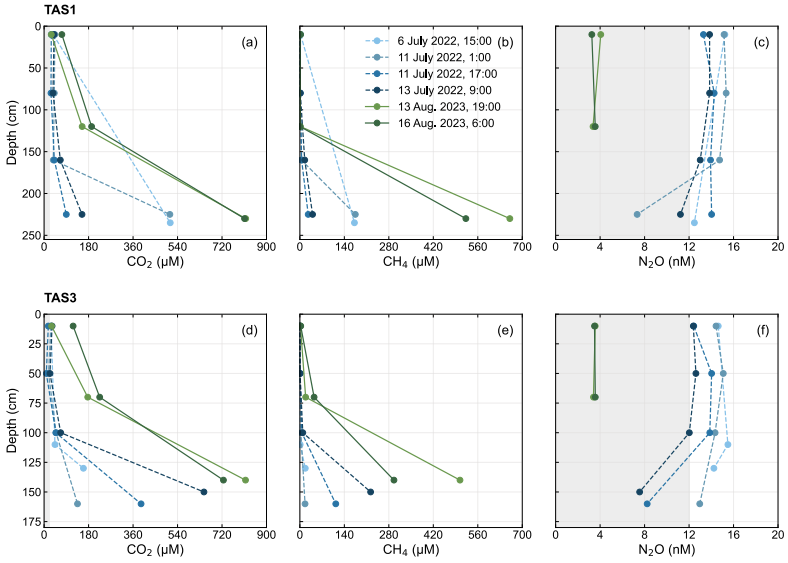

Figure 6. Concentration profiles of CO_2, CH_4 and N_2O from TAS1 (top panels) and TAS3 (bottom panels). Dotted lines represent profiles from 2022, while solid lines represent profiles from 2023. The shaded area represents the concentrations below atmospheric equilibrium values.

Deleted: partial

Deleted: pressure

During the August 2023 campaign, GHG accumulation in the bottom layers led to a steeper vertical gradient. CO_2 concentrations at the bottom were, on average, 12 times higher than at the surface, while bottom CH_4 concentrations were 223 times higher than at the surface. N_2O bottom concentrations were not available in 2023. These gradients resulted in surface gas concentrations that were strongly above air equilibrium for CO_2 and CH_4 but below air equilibrium for N_2O (Table 3). When comparing the two lakes, CO_2 and CH_4 surface concentrations at TAS3 were approximately twice those found at TAS1, despite lower bottom concentrations at TAS3 (Table S5). This difference was again accompanied by a lower pH at TAS3 (Table 2).

Deleted: Table S3,

Overall, the lakes accumulated 2.4 times more CO_2 and 5 times more CH_4 at the bottom in August 2023 compared to July 2022. While bottom N_2O concentrations are unavailable for 2023, concentrations in the middle of the water column were already 3 times lower than those observed in 2022. Surface concentrations of CO_2 and CH_4 were also higher in August 2023 compared to July 2022, while N_2O levels were much lower.

3.5 Summer GHG fluxes

In both years, CO_2 and CH_4 exhibited variable fluxes, with emissions predominantly positive, while N_2O fluxes remained consistently close to equilibrium.

In 2022, CO_2 diffusive fluxes ranged from –2.0 to 17.1 mmol m^{-2} d^{-1}, while CH_4 fluxes ranged from 0.1 to 1.1 mmol m^{-2} d^{-1}, and N_2O fluxes oscillated around zero, never exceeding 0.0036 mmol m^{-2} d^{-1} (Table S3). In terms of CO_2-equivalent emissions, CO_2 accounted for the largest portion of average diffusive emissions, contributing nearly 56% of the total, followed by CH_4 at 41%, and N_2O at only 3.0% (Fig. 7). This analysis excludes ebullition, as it was not assessed in 2022. Average diffusive GHG emissions from TAS1 were five times higher than those from TAS3, consistent with the higher surface concentrations observed at TAS1 as well as the more turbulent conditions (average k_{600} of 3.5 cm h^{-1} at TAS1 and 1.9 cm h^{-1} at TAS3) (Table S6). One of our *k*-estimate was negative (11 July 2022, 17:15 at TAS3; see TableS2), which can happen near equilibrium due to uncertainties in the measurements. This value was excluded from the analysis.

In 2023, CO_2 diffusive fluxes ranged from 7.8 to 67.4 mmol m^{-2} d^{-1}, CH_4 fluxes ranged from 0.3 to 7.2 mmol m^{-2} d^{-1}, and N_2O fluxes ranged from –13.2 to –0.7 mmol m^{-2} d^{-1} (Table S3), resulting from the negative gradients at the air-water interface (Fig. 6). Similar to 2022, CO_2 remained the dominant contributor in terms of CO_2-equivalent diffusive emissions, comprising 64% of total emissions, while CH_4 contributed 39%, and N_2O mitigated total emissions by 4% (sink; Fig. 7). Despite total diffusive fluxes being similar between TAS1 and TAS3 in 2023, surface concentrations of CO_2 and CH_4 were lower at TAS1 (Table 3). This difference is due to the more turbulent conditions at TAS1 (average k_{600} of 5.7 cm h^{-1}), which increased the overall emissions compared to those at TAS3 (average k_{600} of 2.9 cm h^{-1}) (Table S6). Significant CH_4 ebullitive fluxes were recorded at both sites, ranging from 0.5 to 18.1 mmol m^{-2} d^{-1}, while CO_2 ebullitive fluxes remained negligible (Table S3, supplementary dataset). At TAS1, CH_4 ebullitive fluxes were slightly lower than diffusive fluxes, whereas at TAS3, they were more than six times higher than diffusive fluxes on average. Consequently, ebullition accounted for 70% of total emissions at TAS3, primarily driven by CH_4.

Overall, GHG emissions were higher during the intensive campaign period in August 2023 compared to July 2022. The mean diffusive flux of CO_2 was 4.7 times higher, while CH_4 fluxes were almost four times greater. This increase is attributed to higher surface concentrations of both gases (Table 3) and greater turbulence, as indicated by the higher *k* values in 2023 (Table S6). These conditions were reflected on N_2O fluxes, which were consistently negative in 2023, although this flux remains negligible relative to the total flux.

Deleted: S3

Deleted: 11

Formatted: Font: Italic

Deleted: 4

Deleted: This difference is likely due to more turbulent conditions at TAS1

Deleted: , which enhanced overall emissions.

Deleted: see

Formatted: Not Highlight

Deleted: and

Deleted: 4

Deleted: This was also visible at the lake surface, where bubbles accumulated (Fig. S5b).

Deleted: 4

Deleted: **Table 4. Diffusive fluxes of CO_2, CH_4, and N_2O in TAS1 and TAS3 (*N* = 9 in 2022; *N* = 12 in 2023) and ebullitive fluxes of CH_4 in 2023 (*N* = 4 for TAS1; *N* = 8 for TAS3). Values are expressed as mean ± standard deviation (min - max). na = not available.**¶

... [16]

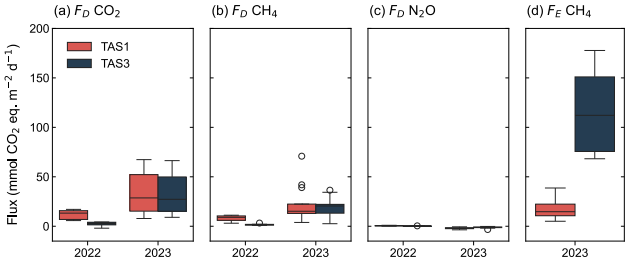

Figure 7. Boxplots of (a) diffusive CO_2 flux, (b) diffusive CH_4 flux, (c) diffusive N_2O flux, and (d) ebullitive CH_4 flux. Fluxes are expressed in mmol CO_2 equivalent m^{-2} d^{-1}, assuming a global warming potential of 27 for CH_4 and 273 for N_2O. Ebullitive flux measurements are only available in summer 2023.

3.6 Summer diel cycles in stratification and diffusive fluxes

During both intensive summer campaigns, clear diel cycles in the buoyancy frequency (N) and dissolved oxygen (DO) were observed (Fig. 8), as indicated by the data collected from the moorings. Although temperature was more variable in 2022 (Fig. S5), peaks in both N and DO typically occurred in the evening (around 18:00), while the lowest values were recorded in the morning (around 07:00). The grey shaded area in the figure indicates periods of zero solar radiation. All data are presented in Eastern Standard Time (EST).

Measurements of CO_2 fluxes, dissolved gas concentrations, and k_{600} over multiple consecutive days across different hours allowed us to reconstruct diel variability for both intensive campaigns (Fig. 9). In 2022, no discernible diel patterns were observed in either the surface concentrations (Fig. S6a,b,c), the gas transfer coefficient (Fig. S7a), or the diffusive emissions of CO_2, CH_4, and N_2O (Fig. 9a,b,c). However, in 2023, distinct diel cycles for diffusive emissions of all three gases emerged (Fig. 9d,e,f), along with the gas transfer coefficient in both lakes, with higher k values observed during the daytime (Fig. S7b). CO_2 fluxes and concentrations exhibited a morning peak between 06:00 and 12:00, followed by a decline to their lowest levels during the evening and night (18:00-03:00; Fig. 9d). CH_4 concentrations were generally higher in the morning and lower at night, though this pattern was less pronounced at TAS1, where concentrations were slightly higher during the day. CH_4 fluxes also displayed a clear diel pattern, with daytime peaks between 09:00 and 18:00 and minima recorded at night (21:00-03:00; Fig. 9e). While N_2O concentrations showed no clear diel trend (Fig. S6d,e,f), N_2O fluxes displayed similar variability to CH_4, with negative fluxes peaking during the day (09:00-18:00) and approaching equilibrium at night (21:00-03:00; Fig. 9f).

Deleted: 6

Deleted: ¶

Formatted: Subscript

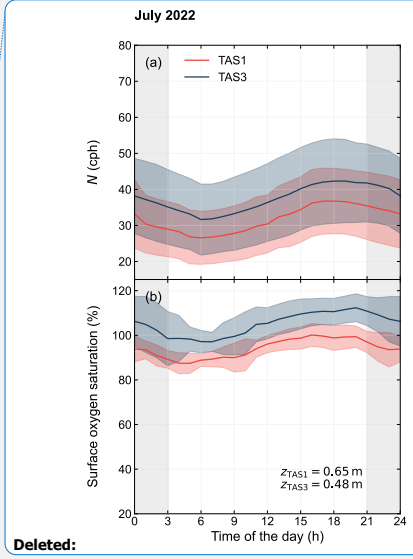

Deleted:

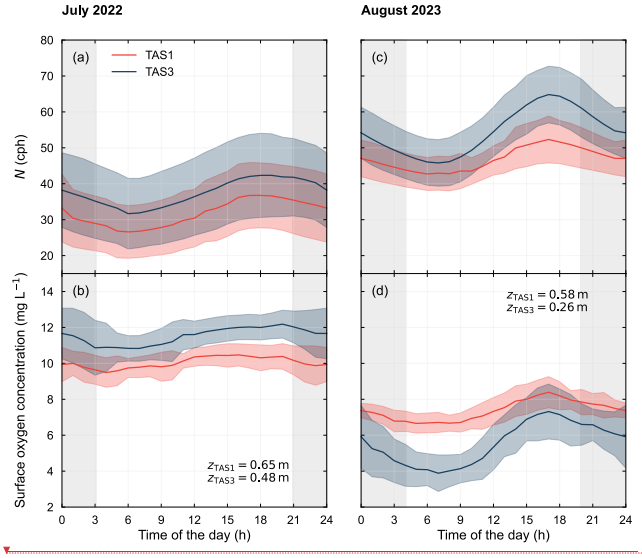

Figure 8. Diel cycles of buoyancy frequency *N* (a,c) and surface dissolved oxygen at depth *z* (c,d) for the July 2022 (left) and August 2023 (right) intensive summer campaign periods. The colored shaded area represents the standard deviation calculated for each hour of the day based on all available measurements within that hour. The grey shaded area indicates periods of zero solar radiation. Time of day is expressed in EST.

Deleted: ¶

Deleted: (in % saturation)

Formatted: Font: (Default) Times New Roman, Font color: Auto

Deleted: , while t

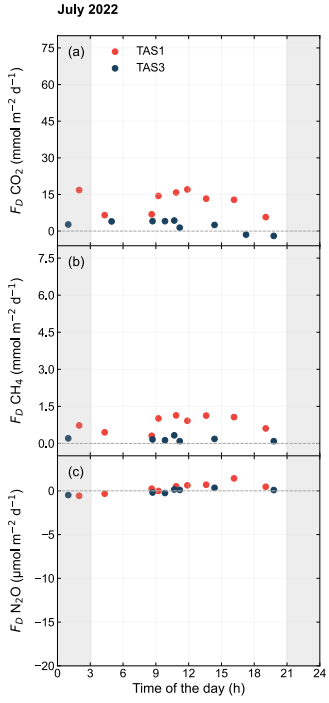

Deleted:

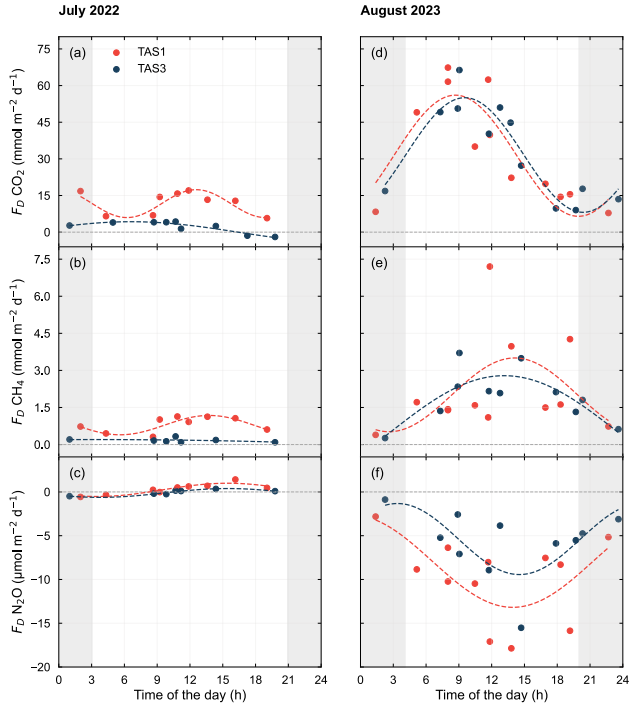

Figure 9. Diel cycles of CO_2 (a,d), CH_4 (b,e) and N_2O (c,f) diffusive fluxes for the July 2022 (left) and August 2023 (right) intensive summer campaign periods. CO_2 fluxes were measured directly with the floating chamber, while CH_4 and N_2O fluxes were obtained by applying the *k* values derived from CO_2 fluxes to their respective concentrations. The grey dotted line represents atmospheric equilibrium, and the grey shaded area indicates periods of zero solar radiation. Although the data are presented on a diurnal cycle, the measurements were taken over a two-week period (see Table S2). Coloured dotted lines represent sine-fitted trend lines. Time of day is expressed in EST.

4 Discussion

The results highlight that GHG emissions from small thermokarst lakes are highly sensitive to interannual variations in meteorological conditions. In this section, we discuss the physicochemical characteristics specific to thermokarst lakes, the summer patterns of dissolved gases and fluxes, and the role of diel and seasonal variability in upscaling lake emissions. Finally, we reflect on the limitations of the study.

Deleted: The grey dotted line represents atmospheric equilibrium.

Deleted: ¶

Deleted: 3.7 Larger-scale estimates¶
The GHG emissions presented so far are based on direct observations but only cover two short-term intensive sampling periods of two weeks each. To better contextualize these fluxes on a seasonal scale, we extend our analysis to encompass broader temporal variations, acknowledging the inherent uncertainties of this approach. Analysis of seasonal variations in GHG diffusive fluxes from lakes TAS1 and TAS3 reveals significant differences in CO_2, CH_4, and N_2O emissions across different periods (Table 5). During the summer of 2022, total GHG fluxes were at their lowest. In the fall of 2022, estimations suggest that both lakes could exhibit substantial increases in emissions, with average fluxes more than 4 times higher in TAS1 and 21 times higher in TAS3 compared to those observed in the previous summer. GHG emission estimates continued to rise in the spring of 2023, particularly for CH_4, which was 10 times higher in TAS1 and 48 times higher in TAS3 than in summer. During the summer of 2023, flux estimates remained elevated, with average fluxes nearly 1.5 times higher in TAS1 and 10.7 times higher in TAS3 compared to summer 2022, although there was greater variability compared to the previous summer. While CH_4 accounted for an average of 41% and 34% of total GHG emissions estimated in summer 2022 and 2023 respectively, its contribution increased to 74% in autumn and 90% in spring. Overall, the highest fluxes were estimated in spring 2023 at TAS3, with average total fluxes of 243.1 mmol CO_2 eq. m^{-2} d^{-1}.¶
¶
Table 5. Seasonal diffusive flux estimates at lakes TAS1 and TAS3. Values are expressed as min - max for each period. na=not available.¶
Lake
The GHG emissions presented so far are based on direct observations but only cover two short-term intensive sampling periods of two weeks each. To better contextualize these fluxes on a seasonal scale, we extend our analysis to encompass broader temporal variations, acknowledging the inherent uncertainties of this approach. Analysis of seasonal variations in GHG diffusive fluxes from lakes TAS1 and TAS3 reveals significant differences in CO_2, CH_4, and N_2O emissions across different periods (Table 5). During the summer of 2022, total GHG fluxes were at their lowest. In the fall of 2022, estimations suggest that both lakes could exhibit substantial increases in emissions, with average fluxes more than 4 times higher in TAS1 and 21 times higher in TAS3 compared to those observed in the previous summer. GHG emission estimates continued to rise in the spring of 2023, particularly for CH_4, which was 10 times higher in TAS1 and 48 times higher in TAS3 than in summer. During the summer of 2023, flux estimates remained elevated, with average fluxes nearly 1.5 times higher in TAS1 and 10.7 times higher in TAS3 compared to summer 2022, although there was greater variability compared to the previous summer. While CH_4 accounted for an average of 41% and 34% of total GHG emissions estimated in summer 2022 and 2023 respectively, its contribution increased to 74% in autumn and 90% in spring. Overall, the highest fluxes were estimated in spring 2023 at TAS3, with average total fluxes of 243.1 mmol CO_2 eq. m^{-2} d^{-1}.¶
¶
Table 5. Seasonal diffusive flux estimates at lakes TAS1 and TAS3. Values are expressed as min - max for each period. na=not available.¶
Lake
... [17]

4.1 Physicochemistry

Thermal stratification in both lakes in summer, despite their shallow depth (< 3 m), reflects strong near-surface absorption of solar radiation driven by low water clarity as well as sheltering from winds. Stratification was more persistent in 2023, coinciding with warmer air temperatures, leading to persistent bottom anoxia. Partial mixing during nighttime cooling eroded this stratification, bringing oxygen-depleted water from deeper layers to the surface, causing surface waters to remain continuously undersaturated with respect to oxygen that summer (Fig. 8). The subsurface oxygen peak, such as the 119% saturation at 100 cm below water surface at TAS1 on 9 August at 15:00, suggest photosynthesis and resistance to mixing. In contrast, 2022 saw cooler, windier conditions that allowed partial mixing and brief bottom reoxygenation. However, oxygen levels quickly returning to anoxic conditions as stability increased (Fig. 3) suggest a high oxygen demand from deeper water and lake sediments. Oxygen supersaturation observed near the surface in TAS3 reflects active photosynthesis and efficient mixing within the surface layer. Overall, the differences observed between the two summers underscore the sensitivity of small lakes to interannual variations in meteorological conditions. Warmer conditions, as observed in 2023, can lead to a rapid onset of spring thermal stratification, potentially preventing the release of gases accumulated during the winter and maintaining a hypoxic lower water column, which allows methane to accumulate more rapidly (e.g., Cortés and Macintyre, 2020).

Lake-specific features further influenced stratification strength and vertical mixing. TAS3, with a_{320} values more than three times higher than at TAS1 in both years (Table 2), absorbed more solar radiation and consistently developed stronger density gradients and shallower mixed layers. Meanwhile, TAS1 experienced more frequent partial mixing (Fig. 3b) and signs of deeper oxygen penetration (Fig. 5b), although differences in sensor placement may have influenced observations, with the logger positioned 58 cm above the bottom at TAS1 compared to 44 cm at TAS3.

Finally, the discrepancy in ice-off dates between lakes in 2023, with TAS3 melting ~2.5 weeks earlier than TAS1, suggests that the ice detection algorithm, which relies on Sentinel-2 imagery, may have missed the actual breakup at TAS1 due to the small size of the lakes and the spatial resolution of 10 m of the imagery. Conductivity data suggest that partial ice melt at TAS1 occurred in mid-May, though not enough to reoxygenate the water, unlike at TAS3. This discrepancy could be due to the higher concentration of CDOM in the ice at TAS3, which could have enhanced sunlight absorption and accelerated melting.

4.2 Summer dissolved gases

The increased supersaturation of CO_2 and CH_4 at the bottom of both lakes during the warmer August 2023 intensive campaign, coupled with the undersaturation of N_2O, underscores the key role of thermal stratification in regulating gas concentrations and vertical gradients. The observed steeper vertical gradients suggest that stratification limited gas evasion to the atmosphere due to reduced mixing and prolonged isolation of the hypolimnion (Fig. 6). Moreover, the rapid onset of thermal stratification after ice cover loss in 2023 (Fig. 3) likely trapped some dissolved gases accumulated during the winter. The increased bottom concentrations of CO_2 and CH_4 in 2023 may also reflect heightened microbial activity and organic matter decomposition in the hypolimnion driven by higher temperatures (see below). While bottom N_2O data were unavailable in 2023, the lower mid-

Deleted: The stratified nature of
Deleted: modest
Deleted: can be attributed to
Formatted: Font: Times New Roman, 10 pt
Formatted: Font: Times New Roman, 10 pt
Formatted: Font: Times New Roman, 10 pt
Deleted: ,
Deleted: observed
Formatted: Font color: Auto
Formatted: Font color: Text 1
Formatted: Font: Times New Roman, 10 pt
Formatted: Font: Times New Roman, 10 pt
Formatted: Font: Times New Roman, 10 pt
Deleted: The low water clarity, marked by high concentrations of solutes and particles (CDOM and TSS), led to enhanced light absorption at the lake surface. This resulted in pronounced surface warming during the day and evening.
Deleted: ¶
¶
Formatted: Font: Times New Roman, 10 pt
¶
¶
Deleted: ¶
Deleted: sampling

water column N_2O concentrations (Fig. 6) suggest that the expanded anoxic water column created favourable conditions for N_2O consumption (Beaulieu et al., 2014), resulting in negative fluxes.

The greater accumulation of GHGs in the lower layers of both lakes in 2023, along with a shallower mixing layer, increased the potential for GHG transport to the surface during mixing and penetrating convection. This, in turn, enhanced both the variability and magnitude of surface GHG accumulation compared to 2022. Notably, the higher GHG concentrations at the surface of TAS3 in 2023 may reflect deeper diurnal mixing, as suggested by lower W values during the day ($1 < W < 10$). Since the mixing layer at TAS3 is shallower than at TAS1 (Fig. 5), wind can more easily disrupt stratification. Additionally, the steeper oxygen gradient in this lake may promote CH_4 production by extending anoxic conditions over a larger portion of the water column. Although photosynthesis and respiration influence CO_2 concentrations through daytime consumption and nighttime production, the large variability in surface concentrations suggests that these processes alone cannot fully explain the observed differences.

The disparities in surface gas concentrations between the two lakes and intensive campaign periods highlight the complexity of the processes governing gas dynamics in thermokarst lakes. Overall, the enhanced GHG accumulation observed during the warmer summer suggests that future climate warming could further amplify GHG buildup in stratified lakes, generating larger seasonal variations.

4.3 Summer GHG fluxes

Studies presenting GHG fluxes from thermokarst lakes and ponds remain scarce. To compare our results with other studies, Table 5 present the reported CO_2 and CH_4 flux from different regions. This non-exhaustive list includes only studies that explicitly identify water bodies formed through thermokarst activity.

In general, our diffusive flux aligns with the range of CO_2 and CH_4 fluxes reported for lakes and ponds in the region. Our results show that under warm and stratified conditions (August 2023), the total diffusive flux was 4 times higher than under colder conditions (July 2022). However, N_2O fluxes were notably lower during this period (higher but negative). Despite the high global warming potential of N_2O (GWP of 273), its uptake had minimal impact on the total GHG fluxes. This pattern is consistent with findings from Davidson et al. (2024), where a shallow eutrophic lake in Denmark acted as a N_2O sink in late summer. Similarly, Bartosiewicz et al. (2016) reported a negligible contribution of N_2O to total GHG emissions from a small, shallow lake in southeastern Canada, where concentrations often remained low or even undersaturated during a heat wave. On the other hand, greater exposure to wind (as in TAS1) resulted in higher k values and higher fluxes, exposing that GHG dynamics can differ significantly between nearby lakes.

The high CH_4 ebullition fluxes recorded are consistent with findings from other studies documenting large CH_4 ebullition flux during the stratified phase (Davidson et al., 2024). The values observed at TAS3, particularly humic and sheltered, are among the highest reported for CH_4 ebullition in Nunavik (Table S3). However, even higher CH_4 ebullition fluxes have been reported from Arctic thermokarst lakes (Table 4). In terms of CO_2-equivalent emissions, CH_4 ebullition at TAS3 contributed 70% of total emissions, compared to 25% at TAS1. The exact reasons for the higher ebullition rates at TAS3 remain unclear, but

Deleted: 6

Deleted: During the warmer intensive campaign in August 2023, the higher surface concentrations of CO2 and CH4, combined with elevated k values (Fig. S8, Table S4), resulted in significantly higher diffusive fluxes for both gases compared to the colder intensive campaign in July 2022. Thus, t

Formatted: Font color: Text 1

Formatted: Font: (Default) Times New Roman, 10 pt, Font color: Text 1

Deleted: in August 2023

Deleted: in

Formatted: Font: (Default) Times New Roman, 10 pt, Font color: Text 1

Formatted: Font color: Text 1

Deleted: . In contrast

Deleted: ,

Deleted: , driven by reduced concentrations and a slightly negative gradient at the air-water interface

Deleted: In 2022, the higher fluxes at TAS1 corresponded to both higher surface concentrations and higher *k* values compared to TAS3. However, in 2023, fluxes were similar between the lakes, despite significantly higher surface concentrations at TAS3 (Table 3). This can be attributed to the h

Deleted: at TAS1 (Fig. S8), likely driven by greater exposure to wind, …

Deleted: which compensated for its lower surface concentrations

Deleted: . Thus,

Deleted: , and large-scale estimates and comparisons should account for these spatial differences.

Formatted: Font:

Deleted: H

Deleted: were

Deleted: in 2023, particularly in TAS3,

Deleted: 5

Deleted: 6

several factors may contribute. One possibility is its higher organic content, with bottom DOC levels nearly three times higher than at TAS1 (Table 2), potentially reflecting a higher microbial productivity. Plankton was abundant in TAS3 (though not analyzed), and the presence of dense shrub cover along its shores suggests that falling leaves contribute organic material to the water column and sediment, fueling methanogenic activity (Heslop et al., 2015). However, we acknowledge that our estimates of CH_4 ebullition were based on measurements from a single funnel deployed at the lake center. This methodological choice limits the spatial representativity of the results and may partially explain the differences observed between the lakes, especially since ebullition is known to be highly heterogeneous, with localized hotspots often occurring near lake edges or thawing permafrost zones (Wik et al., 2011; Kuhn et al., 2023). Future studies should aim to include multiple bubble traps across various lake zones to capture this heterogeneity and better constrain whole-lake ebullition estimates.

While both intensive campaign periods occurred during the summer season, we acknowledge that they were conducted at different times, with the 2023 campaign occurring later in the season. Beyond the overall differences in environmental conditions between both summers–2022 being colder than 2023– the timing of sampling may have captured distinct seasonal phases. Late summer is typically characterized by a warmer water column and greater accumulation of GHGs at the bottom due to prolonged stratification throughout the season (Prėskienis et al., 2021).

Formatted: Font: (Default) Times New Roman, Not Bold, Font color: Text 1

Formatted: Subscript

Formatted: Font: (Default) Times New Roman, Not Bold, Font color: Text 1

Formatted: Font: (Default) Times New Roman, Not Bold, Font color: Text 1

Deleted: (Wik et al., 2011; Kuhn et al., 2023)

Deleted:

Deleted: ~~Additionally, it could reflect methodological biases caused by large spatial variations in CH_4 bubbling, as highlighted by Wik et al. (2011) in their study of larger Arctic lakes in Sweden.~~

Deleted: ~~Although ebullitive fluxes were not measured in 2022, we hypothesize they were lower, as no visible bubbles were observed at the lake surface, in contrast to the frequent bubbling seen in 2023 on calm days (Fig. S5). Moreover, the bottom water temperature at TAS1 was 2.1°C colder in July 2022 compared to August 2023 (5.7°C vs 7.8°C), while at TAS3 it was 3.8°C colder (5.1°C vs 8.9°C). Given that heat flux into lakes has been identified as a key driver of gas production and release in Swedish lakes (Wik et al., 2014), these temperature differences may have contributed to the observed variations in bubbling activity.~~

Deleted: (0.7°C above seasonal normal)

Deleted: (2.6°C above seasonal normal)

Deleted: ¶

Deleted: 6

Table 5. Reported CO_2 and CH_4 fluxes from thermokarst lakes and ponds. Negative values represent uptake from the atmosphere. Nb is the number of waterbodies studied. Type of permafrost are continuous (C), discontinuous (D) and sporadic (S). Methods for acquiring diffusive flux are chamber (CH), headspace equilibration (HS), sensors measuring concentration directly in the field (SR), bubble traps (BT) and wind models (WM). na=not available

				Reported fluxes (mmol m^{-2} d^{-1})				
Site	Reference	Region	Nb	$F_{D\,CO_2}$	$F_{E\,CO_2}$	$F_{D\,CH_4}$	$F_{E\,CH_4}$	Method
Nunavik, Canada	This study	D; Lithalsa	2	21.6 (–2.0 - 67.4)	0.2 (0.0 - 0.3)	1.5 (0.1 - 7.2)	9.6 (0.5 - 25.2)	CH, HS, BT
	Matveev et al. (2018)	D, S; Lithalsa	8	12.3 (–1.7 - 30.8)	0.1 (0.006 - 0.2)	0.4 (0.07 - 0.82)	0.1 (0.02 - 0.25)	HS, SR, WM, BT
	Matveev et al. (2016)	D, S; Palsa	9	58.3 (4 - 242)	0.01 (0.001 - 0.1)	3.3 (0.01 - 12.8)	0.2 (<0.01 - 0.8)	HS, SR, WM, BT
Nunavut, Canada	Prėskienis et al. (2021)[1]	C; High Arctic ice-wedge	21	7.1	0.1	0.4	0.9	HS, WM
Northernmost Alberta, Canada	Kuhn et al. (2023)	S; Boreal	1	na	0.54	2.56	8.21	BT, HS, WM
Tibetan Plateau, Central Asia	Wang et al. (2021)	C, D and S; Alpine	32	na	na	2.6 (0.003 - 48.4)	6.6 (0.002 - 140.0)	HS, WM, CH
	Yang et al. (2023)	D and S; Alpine	120	170.3 (–33.7 - 445.0)	na	2.1 (0.1 - 7.9)	11.2 (0.03 - 31.4)	CH, HS
Central Yakutia, Eastern Siberia	Hughes-Allen et al. (2021)	C; Peatland	91	19.9 (–9.4 - 355.4)	na	19.9 (0.1 - 566.4)	na	HS, WM

[1] Kettle lakes in Prėskienis et al. (2021) were later identified by Coulombe et al. (2022) as glacial thermokarst lakes and thus were included in the average grouping ice-wedge trough ponds, ice-wedge thermokarst lakes, and glacial thermokarst lakes

4.4 The importance of diel variability in upscaling emissions

Estimates of GHG emissions from lakes often rely on daytime measurements, but our findings indicate that this approach can significantly overestimate total 24-hour fluxes. Numerous studies also reported diel variability in subtropical lakes (Zhao et al., 2024), boreal and temperate lakes (Sieczko et al., 2020; Erkkilä et al., 2018; Podgrajsek et al., 2014; Martinez-Cruz et al., 2020), subarctic lakes (Jammet et al., 2017), glacial lake (Eugster et al., 2022) as well as across multiple sites in the Northern Hemisphere (Golub et al., 2023). In 2023, the pronounced diel pattern in surface gas concentrations and k led to significantly higher daytime (9:00-17:00) diffusive fluxes: 47% higher for CO_2, 95% for CH_4, and 75% for N_2O (negative fluxes for N_2O; Fig. 9). Notably, this pattern was not observed in July 2022, likely due to the colder weather and weaker stratification following an recent mixing event, which may have resulted in gas venting (Fig. 3). The drivers of diel GHG emission patterns are multifaceted, involving both physical (mixing patterns) and biological factors (production vs. consumption rates), though the latter were not explored in this study. For instance, the decline in surface oxygen observed ~3 hours after sunrise (Fig. 8) may be attributed to increasing morning winds, which promote vertical mixing, combined with ongoing respiration that outpaces photosynthesis early in the day.

Our results show that the high morning CO_2 fluxes were primarily driven by elevated gas concentrations in the upper water column, illustrated by the significant correlation between flux and departure from saturation ($r = 0.49$, $p = 0.018$). The higher morning CO_2 concentrations coincided with weaker stratification and lower oxygen levels at that time (Fig. S6d, Fig. 8c,d). The rapid decrease from noon was likely due to increased photosynthetic activity driven by solar radiation (which peaks around 12:00; Fig. S5) and reduced CO_2 solubility as daytime temperatures rose. This pattern aligns with findings from Arctic thermokarst lakes (Prėskienis et al., 2021), where nighttime respiration and daytime photosynthesis, along with nighttime convective mixing, were suggested to concurrently drive CO_2 and O_2 dynamics by bringing GHG-enriched, oxygen-depleted water from deeper layers to the surface (Walter Anthony and Macintyre, 2016). Similarly, elevated morning CO_2 concentrations have been reported in a boreal humic lake, where surface concentrations were strongly influenced by the stability of stratification (Huotari et al., 2009).

Wind-induced turbulence played a dominant role in controlling fluxes of CH_4 and N_2O, as these gases were more closely linked to k patterns ($r = 0.78$, $p < 0.001$; $r = -0.98$, $p < 0.001$ for CH_4 and N_2O respectively), with their surface concentrations remaining relatively stable. However, CH_4 in TAS3 followed a pattern similar to CO_2, highlighting the need for additional measurements to better resolve these diel patterns. Wind-driven dynamics contributing to higher daytime fluxes have also been reported in boreal lakes (Sieczko et al., 2020). These differing dynamics caused CH_4 and N_2O fluxes to peak later in the day compared to CO_2. This contrasts with findings from Eugster et al. (2020), who reported elevated CO_2 and CH_4 fluxes at night (2h-6h) in a deep glacial lake, and Podgrajsek et al. (2014), who observed high CH_4 fluxes during the night and early morning (00h-08h) in a boreal lake, both coinciding with periods of strongest surface cooling and convection. These results highlight the importance of conducting full 24-hour sampling in order to accurately capture GHG emissions from lakes, not only in biologically productive systems, but also in high-latitude thermokarst environments. Despite their small size and shallow depth,

Deleted: Estimates of GHG emissions from lakes often rely on daytime measurements, but our finding indicate that this approach can significantly overestimate total 24-hour fluxes, as observed by Sieczko et al. (2020) in boreal lakes and Martinez-Cruz et al. (2020) in eutrophic temperate lakes using automated chambers.

Formatted: Font color: Text 1

Formatted: Font: Not Bold, Font color: Text 1

Deleted: T

Deleted: a colder period characterized by

Deleted: intensive

Deleted: period

Deleted: likely

Deleted: ¶

Deleted: causes

Deleted: these

Formatted: Font:

Deleted: Wind-induced turbulence and convective mixing play a key role by redistributing gas-rich, low-oxygen water from the lower layers to the surface.

Deleted: ¶

Formatted: Font: (Default) Times New Roman, 10 pt, Font color: Text 1

Formatted: Font: (Default) Times New Roman, 10 pt, Font color: Text 1

Deleted: Then, solar heating promotes stratification, progressively isolating bottom waters and influencing daily flux dynamics.

Formatted: Font:

Deleted: suggest

Deleted: , combined with an increase in turbulence (k) during the day. …

Deleted: 7

Deleted: .

Deleted: 6

Deleted: ¶

Formatted: Font: Italic

Formatted: Font: Italic

Formatted: Subscript

Formatted: Subscript

these lakes exhibit pronounced diel patterns in stratification and oxygen dynamics, demonstrating that GHG fluxes are largely driven by physical processes. Furthermore, the distinctive light regimes of the Arctic and sub-Arctic regions, characterised by prolonged daylight hours, could intensify stratification during the summer. This emphasises the importance of considering latitude-specific dynamics when evaluating lake GHG budgets.

4.5 Larger-scale estimates and limitations

While our GHG flux measurements are limited to two intensive summer campaigns, we recognize that emissions from thermokarst lakes can vary substantially beyond these short observation windows. In particular, the accumulation of CO_2 and CH_4 in bottom waters during summer and winter stratification may lead to substantial emissions during spring and fall turnover events. To explore the potential scale of these seasonal variations, we performed an indicative extrapolation of diffusive GHG fluxes using seasonal limnophysical data and dissolved gas concentrations measured in the water columns during summer. The methodological approach and detailed results are provided in the Supplementary Material (Table S7, S8 and S9) and should be interpreted with caution given the simplifying assumptions and lack of direct flux measurements outside summer.

The larger scale estimate analysis suggests that GHG fluxes may peak during spring and fall, particularly at TAS3, where stronger stratification allowed for greater gas buildup at the bottom. CH_4 was the dominant contributor to these estimated peak fluxes when mixing likely released stored gases. The larger GHG fluxes estimated during the summer of 2023 compared to summer 2022 reflects enhanced stratification and intensified decomposition processes, leading to greater accumulation and subsequent release of CO_2 and CH_4. While we were unable to estimate k during the fall 2023 and spring 2024 periods, it is likely that fluxes would have been substantially higher due to the higher buildup of GHG at the bottom (Table S8). Overall, these findings emphasize the potential magnitude of emissions outside the summer period and highlight the importance of monitoring GHG fluxes year-round to gain a deeper understanding of the dynamics and drivers behind seasonal emission patterns.

Several factors should be considered to improve the accuracy of GHG flux estimates. First, under calm conditions, microstratification can slow the vertical exchange of gases even within the top few centimeters of the water column (Aurich et al., 2025) demonstrated that CO_2 concentrations may vary significantly between 5 and 25 cm depth during windless periods, with the surface being supersaturated. When quantifying gas concentration with the headspace method, water is typically collected from the upper 10-20 cm, which could overestimate concentrations at the very surface during warm, calm periods, potentially inflating flux estimates when applying a gas transfer model. In contrast, all measurements in the present study were conducted at the lake centre, which may have led to an underestimation of fluxes. Previous studies, such as Kuhn et al. (2023), have shown that diffusive fluxes near the edges can be significantly higher (twice in their study) than at the centre. Finally, with only one funnel used per lake to measure ebullition, we may have missed localized high-ebullition sites, particularly near the edges, despite the lakes being very small. For instance, Kuhn et al. (2023) reported CH_4 ebullition fluxes up to four times higher at the thawing edges of thermokarst lakes compared to the lake centre.

Formatted: Font color: Text 1
Formatted: Font color: Text 1
Deleted: 4
Formatted: Font color: Text 1, Subscript
Formatted: Font color: Text 1, Subscript
Formatted: Font color: Text 1
Formatted: Font color: Text 1, Subscript
Formatted: Font color: Text 1
Formatted: Font: Italic, Font color: Text 1
Formatted: Font color: Text 1
Formatted: Font color: Text 1
Deleted: in cases of
Deleted: strong
Deleted: stratification (as in 2023), gas concentration gradients may be pronounced even near the surface
Deleted:
Formatted: Font: Times New Roman, 10 pt, Font color: Text 1
Formatted: Font color: Text 1
Formatted: Font color: Text 1
Formatted: Font: Times New Roman, 10 pt, Font color: Text 1
Formatted: Font color: Text 1, Subscript
Formatted: Font: Times New Roman, 10 pt, Font color: Text 1
Formatted: Font color: Text 1
Deleted: , especially
Deleted: during the day
Deleted: Conversly
Deleted: taken
Deleted: could
Deleted: result in
Formatted: Font color: Text 1
Deleted: (despite the lakes being very small)
Formatted: Font color: Text 1
Formatted: Font color: Text 1
Formatted: Font color: Text 1

5 Conclusions

In this study, two thermokarst lakes–one more humic and sheltered and the other more transparent and wind-exposed–were monitored for nearly two years, with continuous measurements of temperature, oxygen, and conductivity. These long-term observations were complemented by GHG flux and concentration measurements from two intensive summer campaigns–one colder and the other warmer–to quantify emissions and their variability. The thermokarst lakes were significant emitters of CO_2 and CH_4, with lake N_2O uptake only minimally offsetting these emissions. Our results show large temporal variations in GHG fluxes during the warm intensive campaign in 2023, with peak CO_2 fluxes occurring in the morning and peak CH_4 and N_2O fluxes observed later in the day. The differences observed between the warmer and the cooler intensive campaigns were partly due to the mixing regime and the accumulation of dissolved gases in the water column. Stratification allowed for the buildup of dissolved GHGs, which were then brought to the surface during nighttime cooling and mixing, subsequently released to the atmosphere as wind speeds rose. Notably, ebullitive CH_4 fluxes were predominant in the more humic and sheltered lake, which receives organic inputs from leafy shrubs, illustrating the potential differences between two adjacent lakes. While our seasonal flux estimates suggest that emissions may peak in fall and spring, highlighting the role of GHG storage and release in stratified water bodies, these remain speculative, as direct seasonal GHG measurements were not conducted. This highlights the importance of long-term monitoring that accounts for both seasonal and diel patterns in emissions, alongside the environmental factors that regulate the efficiency of lake mixing and GHG production and consumption.

Data availability. The datasets generated and/or analysed during this study are available on Borealis, the Canadian Dataverse Repository at https://doi.org/10.5683/SP3/KCX9KV.

Author contributions. IL and AP planned the campaign; AT installed the buoy and sensor system; AP, IL and AT conducted the measurements; AP analysed the data; AP wrote the manuscript, with all authors providing feedback on earlier drafts and approving the final version.

Competing interests. The contact author has declared that none of the authors has any competing interests.

Acknowledgements. We would like to express our sincere gratitude to the Inuit community of Umiujaq for granting permission to work in the study area. Our thank also go to Jean-Michel Lemieux for his invaluable insights into the evolution of thermokarst lakes in the Tasiapik Valley, as well as to Denis Sarrazin and Florent Dominé for providing key data for this study. We are also grateful to Geneviève Beaudoin and Clarence Gagnon for their essential field assistance.

Deleted: ¶

Deleted: will

Deleted: be

Financial support. This project was funded by the Université Laval Sentinel North program (DN) and the NSERC Discovery grant (IL), with additional logistical support from the Centre d'Études Nordiques (CEN).

References

Abnizova, A., Siemens, J., Langer, M., and Boike, J.: Small ponds with major impact: The relevance of ponds and lakes in permafrost landscapes to carbon dioxide emissions, Global Biogeochem. Cy., 26, GB2041, 10.1029/2011GB004237, 2012.

Aurich, P., Spank, U., and Koschorreck, M.: Surface CO_2 gradients challenge conventional CO_2 emission quantification in lentic water bodies under calm conditions, Biogeosciences, 22, 1697-1709, 10.5194/bg-22-1697-2025, 2025.

Bartosiewicz, M., Laurion, I., Clayer, F., and Maranger, R.: Heat-wave effects on oxygen, nutrients, and phytoplankton can alter global warming potential of gases emitted from a small shallow lake, Environ. Sci. Technol., 50, 6267-6275, 10.1021/acs.est.5b06312, 2016.

Beaulieu, J. J., Smolenski, R. L., Nietch, C. T., Townsend-Small, A., Elovitz, M. S., and Schubauer-Berigan, J. P.: Denitrification alternates between a source and sink of nitrous oxide in the hypolimnion of a thermally stratified reservoir, Limnol. Oceanogr., 59, 495-506, 10.4319/lo.2014.59.2.0495, 2014.

Begin, P. N., Tanabe, Y., Rautio, M., Wauthy, M., Laurion, I., Uchida, M., Culley, A. I., and Vincent, W. F.: Water column gradients beneath the summer ice of a High Arctic freshwater lake as indicators of sensitivity to climate change, Scientific Reports, 11, 2868, 10.1038/s41598-021-82234-z, 2021.

Bouchard, F., Laurion, I., Prekienis, V., Fortier, D., Xu, X., and Whiticar, M. J.: Modern to millennium-old greenhouse gases emitted from ponds and lakes of the Eastern Canadian Arctic (Bylot Island, Nunavut), Biogeosciences, 12, 7279-7298, 10.5194/bg-12-7279-2015, 2015.

Burke, S. A., Wik, M., Lang, A., Contosta, A. R., Palace, M., Crill, P. M., and Varner, R. K.: Long-Term Measurements of Methane Ebullition From Thaw Ponds, J. Geophys. Res.-Biogeosciences, 124, 2208-2221, 10.1029/2018JG004786, 2019.

Bussière, L., Schmutz, M., Fortier, R., Lemieux, J. M., and Dupuy, A.: Near-surface geophysical imaging of a thermokarst pond in the discontinuous permafrost zone in Nunavik (Québec), Canada, Permafrost Periglac., 33, 353-369, 10.1002/ppp.2166, 2022.

CEN: Données des stations climatiques d'Umiujaq au Nunavik, Québec, Canada, v. 1.9.0 (1997-2023). Nordicana D9 [dataset], 10.5885/45120SL-067305A53E914AF0, 2024.

Cole, J. J. and Caraco, N. F.: Atmospheric exchange of carbon dioxide in a low-wind oligotrophic lake measured by the addition of SF6, Limnol. Oceanogr., 43, 647-656, 10.4319/lo.1998.43.4.0647, 1998.

Collins, A.: Properties of produced waters, in: Petroleum engineering handbook, Society of Petroleum Engineers, Richardson, Texas, 1987.

Cortés, A. and MacIntyre, S.: Mixing processes in small arctic lakes during spring, Limnol. Oceanogr., 65, 260-288, 10.1002/lno.11296, 2020.

Coulombe, S., Fortier, D., Bouchard, F., Paquette, M., Charbonneau, S., Lacelle, D., Laurion, I., and Pienitz, R.: Contrasted geomorphological and limnological properties of thermokarst lakes formed in buried glacier ice and ice-wedge polygon terrain, The Cryosphere, 16, 2837-2857, 10.5194/tc-16-2837-2022, 2022.

Crevecoeur, S., Vincent, W. F., Comte, J., and Lovejoy, C.: Bacterial community structure across environmental gradients in permafrost thaw ponds: methanotroph-rich ecosystems, Front. Microbiol., 6, 192, 10.3389/fmicb.2015.00192, 2015.

Dagenais, S., Molson, J., Lemieux, J. M., Fortier, R., and Therrien, R.: Coupled cryo-hydrogeological modelling of permafrost dynamics near Umiujaq (Nunavik, Canada), Hydrogeol. J., 28, 887-904, 10.1007/s10040-020-02111-3, 2020.

Davidson, T. A., Søndergaard, M., Audet, J., Levi, E., Esposito, C., Bucak, T., and Nielsen, A.: Temporary stratification promotes large greenhouse gas emissions in a shallow eutrophic lake, Biogeosciences, 21, 93-107, 10.5194/bg-21-93-2024, 2024.

Domart, D., Nadeau, D. F., Thiboult, A., Anctil, F., Ghobrial, T., Prairie, Y. T., Bédard-Therrien, A., and Tremblay, A.: A global analysis of ice phenology for 3702 lakes and 1028 reservoirs across the Northern Hemisphere using Sentinel-2 imagery, Cold Reg. Sci. Technol., 227, 104294, 10.1016/j.coldregions.2024.104294, 2024.

Downing, J. A.: Emerging global role of small lakes and ponds: little things mean a lot, Limnética, 29, 9-24, 10.23818/limn.29.02, 2010.

Erkkilä, K. M., Ojala, A., Bastviken, D., Biermann, T., Heiskanen, J. J., Lindroth, A., Peltola, O., Rantakari, M., Vesala, T., and Mammarella, I.: Methane and carbon dioxide fluxes over a lake: comparison between eddy covariance, floating chambers and boundary layer method, Biogeosciences, 15, 429-445, 10.5194/bg-15-429-2018, 2018.

Eugster, W., DelSontro, T., Shaver, G. R., and Kling, G. W.: Interannual, summer, and diel variability of CH_4 and CO_2 effluxes from Toolik Lake, Alaska, during the ice-free periods 2010–2015, Environm. Sci.-Proc. Imp., 22, 2181-2198, 10.1039/d0em00125b, 2020.

Eugster, W., DelSontro, T., Laundre, J. A., Dobkowski, J., Shaver, G. R., and Kling, G. W.: Effects of long-term climate trends on the methane and CO_2 exchange processes of Toolik Lake, Alaska, Front. Env. Sci., 10, 10.3389/fenvs.2022.948529, 2022.

Fortier, R., Banville, D.-R., Lévesque, R., Lemieux, J.-M., Molson, J., Therrien, R., and Ouellet, M.: Development of a three-dimensional geological model, based on Quaternary chronology, geological mapping, and geophysical investigation, of a watershed in the discontinuous permafrost zone near Umiujaq (Nunavik, Canada), Hydrogeol. J., 28, 813-832, 10.1007/s10040-020-02113-1, 2020.

Golub, M., Koupaei-Abyazani, N., Vesala, T., Mammarella, I., Ojala, A., Bohrer, G., Weyhenmeyer, G. A., Blanken, P. D., Eugster, W., Koebsch, F., Chen, J., Czajkowski, K., Deshmukh, C., Guérin, F., Heiskanen, J., Humphreys, E., Jonsson, A., Karlsson, J., Kling, G., Lee, X., Liu, H., Lohila, A., Lundin, E., Morin, T., Podgrajsek, E., Provenzale, M., Rutgersson, A., Sachs, T., Sahlée, E., Serça, D., Shao, C., Spence, C., Strachan, I. B., Xiao, W., and Desai, A. R.: Diel, seasonal, and inter-annual variation in carbon dioxide effluxes from lakes and reservoirs, Environm. Res. Lett., 18, 034046, 10.1088/1748-9326/acb834, 2023.

Goodrich, J. P., Varner, R. K., Frolking, S., Duncan, B. N., and Crill, P. M.: High-frequency measurements of methane ebullition over a growing season at a temperate peatland site, Geophys. Res. Lett., 38, L07404, 10.1029/2011GL046915, 2011.

Greene, S., Walter Anthony, K. M., Archer, D., Sepulveda-Jauregui, A., and Martinez-Cruz, K.: Modeling the impediment of methane ebullition bubbles by seasonal lake ice, Biogeosciences, 11, 6791-6811, 10.5194/bg-11-6791-2014, 2014.

Grosse, G., Jones, B., and Arp, C.: Thermokarst Lakes, Drainage, and Drained Basins, in: Treatise on Geomorphology, edited by: Shroder, J. F., Academic Press, San Diego, USA, 325-353, 10.1016/B978-0-12-374739-6.00216-5, 2013.

Heslop, J., Walter Anthony, K. M., Sepulveda-Jauregui, A., Martinez-Cruz, K., Bondurant, A., Grosse, G., and Jones, M. C.: Thermokarst lake methanogenesis along a complete talik profile, Biogeosciences, 12, 4317-4331, 10.5194/bg-12-4317-2015, 2015.

Heslop, J. K., Walter Anthony, K. M., Winkel, M., Sepulveda-Jauregui, A., Martinez-Cruz, K., Bondurant, A., Grosse, G., and Liebner, S.: A synthesis of methane dynamics in thermokarst lake environments, Earth-Sci. Reviews, 210, 103365, 10.1016/j.earscirev.2020.103365, 2020.

Holgerson, M. A., Zappa, C. J., and Raymond, P. A.: Substantial overnight reaeration by convective cooling discovered in pond ecosystems, Geophys. Res. Lett., 43, 8044-8051, 10.1002/2016GL070206, 2016.

Hughes-Allen, L., Bouchard, F., Laurion, I., Séjourné, A., Marlin, C., Hatté, C., Costard, F., Fedorov, A., and Desyatkin, A.: Seasonal patterns in greenhouse gas emissions from thermokarst lakes in Central Yakutia (Eastern Siberia), Limnol. Oceanogr., 66, S98-S116, 10.1002/lno.11665, 2021.

Huotari, J., Ojala, A., Peltomaa, E., Pumpanen, J., Hari, P., and Vesala, T.: Temporal variations in surface water CO_2 concentration in a boreal humic lake based on high-frequency measurements, Boreal Env. Res., 14, 48-60, 2009.

Huttunen, J. T., Väisänen, T. S., Heikkinen, M., Hellsten, S., Nykänen, H., Nenonen, O., and Martikainen, P. J.: Exchange of CO_2, CH_4 and N_2O between the atmosphere and two northern boreal ponds with catchments dominated by peatlands or forests, Plant soil, 242, 137-146, 10.1023/A:1019606410655, 2002.

IPCC: Climate Change 2023: Synthesis Report. Contribution of Working Groups I, II and III to the Sixth Assessment Report of the Intergovernmental Panel on Climate Change., 184 pp., IPCC, Geneva, Switzerland, Core Writing Team and Lee, H. and Romero, J. edn., 10.59327/IPCC/AR6-9789291691647, 2023.

Jähne, B., Heinz, G., and Dietrich, W.: Measurement of the diffusion coefficients of sparingly soluble gases in water, J. Geophys. Res.-Oceans, 92, 10767-10776, 10.1029/JC092iC10p10767, 1987.

Jammet, M., Dengel, S., Kettner, E., Parmentier, F. J. W., Wik, M., Crill, P., and Friborg, T.: Year-round CH_4 and CO_2 flux dynamics in two contrasting freshwater ecosystems of the subarctic, Biogeosciences, 14, 5189-5216, 10.5194/bg-14-5189-2017, 2017.

Jolivel, M. and Allard, M.: Thermokarst and export of sediment and organic carbon in the Sheldrake River watershed, Nunavik, Canada, J. Geophys. Res.-Earth Surface, 118, 1729-1745, 10.1002/jgrf.20119, 2013.

Jones, F. E. and Harris, G. L.: ITS-90 density of water formulation for volumetric standards calibration, J. Res. Natl. Inst. Stand. Technol., 97, 335, 1992.

Kuhn, M. A., Thompson, L. M., Winder, J. C., Braga, L. P., Tanentzap, A. J., Bastviken, D., and Olefeldt, D.: Opposing effects of climate and permafrost thaw on CH_4 and CO_2 emissions from northern lakes, AGU Advances, 2, e2021AV000515, 10.1029/2021AV000515, 2021.

Kuhn, M. A., Schmidt, M., Heffernan, L., Stührenberg, J., Knorr, K.-H., Estop-Aragonés, C., Broder, T., Gonzalez Moguel, R., Douglas, P. M. J., and Olefeldt, D.: High ebullitive, millennial-aged greenhouse gas emissions from thermokarst expansion of peatland lakes in boreal western Canada, Limnol. Oceanogr., 68, 498-513, 10.1002/lno.12288, 2023.

Laurion, I., Vincent, W. F., MacIntyre, S., Retamal, L., Dupont, C., Francus, P., and Pienitz, R.: Variability in greenhouse gas emissions from permafrost thaw ponds, Limnol. Oceanogr., 55, 115-133, 10.4319/lo.2010.55.1.0115, 2010.

Lemieux, J.-M., Fortier, R., Talbot-Poulin, M.-C., Molson, J., Therrien, R., Ouellet, M., Banville, D., Cochand, M., and Murray, R.: Groundwater occurrence in cold environments: examples from Nunavik, Canada, Hydrogeol. J., 24, 1497-1513, 10.1007/s10040-016-1411-1, 2016.

MacIntyre, S., Jonsson, A., Jansson, M., Aberg, J., Turney, D. E., and Miller, S. D.: Buoyancy flux, turbulence, and the gas transfer coefficient in a stratified lake, Geophys. Res. Lett., 37, L24604, 10.1029/2010GL044164, 2010.

MacIntyre, S., Bastviken, D., Arneborg, L., Crowe, A. T., Karlsson, J., Andersson, A., Gålfalk, M., Rutgersson, A., Podgrajsek, E., and Melack, J. M.: Turbulence in a small boreal lake: Consequences for air–water gas exchange, Limnol. Oceanogr., 66, 827-854, 10.1002/lno.11645, 2021.

Martinez-Cruz, K., Sepulveda-Jauregui, A., Greene, S., Fuchs, A., Rodriguez, M., Pansch, N., Gonsiorczyk, T., and Casper, P.: Diel variation of CH_4 and CO_2 dynamics in two contrasting temperate lakes, Inland Waters, 10, 333-347, 10.1080/20442041.2020.1728178, 2020.

Matveev, A., Laurion, I., and Vincent, W. F.: Methane and carbon dioxide emissions from thermokarst lakes on mineral soils, Arctic Science, 4, 584-604, 10.1139/as-2017-0047, 2018.

Matveev, A., Laurion, I., Deshpande, B. N., Bhiry, N., and Vincent, W. F.: High methane emissions from thermokarst lakes in subarctic peatlands, Limnol. Oceanogr., 61, S150-S164, 10.1002/lno.10311, 2016.

Podgrajsek, E., Sahlée, E., and Rutgersson, A.: Diurnal cycle of lake methane flux, J. Geophys. Res.-Biogeosciences, 119, 236-248, 10.1002/2013JG002327, 2014.

Prėskienis, V., Laurion, I., Bouchard, F., Douglas, P. M. J., Billett, M. F., Fortier, D., and Xu, X.: Seasonal patterns in greenhouse gas emissions from lakes and ponds in a High Arctic polygonal landscape, Limnol. Oceanogr., 66, S117-S141, 10.1002/lno.11660, 2021.

Schuur, E. A. G., Vogel, J. G., Crummer, K. G., Lee, H., Sickman, J. O., and Osterkamp, T. E.: The effect of permafrost thaw on old carbon release and net carbon exchange from tundra, Nature, 459, 556-559, 10.1038/nature08031, 2009.

Sepulveda-Jauregui, A., Walter Anthony, K. M., Martinez-Cruz, K., Greene, S., and Thalasso, F.: Methane and carbon dioxide emissions from 40 lakes along a north–south latitudinal transect in Alaska, Biogeosciences, 12, 3197-3223, 10.5194/bg-12-3197-2015, 2015.

Serikova, S., Pokrovsky, O. S., Laudon, H., Krickov, I. V., Lim, A. G., Manasypov, R. M., and Karlsson, J.: High carbon emissions from thermokarst lakes of Western Siberia, Nat. Commun., 10, 1552, 10.1038/s41467-019-09592-1, 2019.

Sieczko, A. K., Duc, N. T., Schenk, J., Pajala, G., Rudberg, D., Sawakuchi, H. O., and Bastviken, D.: Diel variability of methane emissions from lakes, P. Natl. A. Sci., 117, 21488-21494, 10.1073/pnas.2006024117, 2020.

Smith, L. C., Sheng, Y., MacDonald, G. M., and Hinzman, L. D.: Disappearing Arctic Lakes, Science, 308, 1429-1429, 10.1126/science.1108142, 2005.

Tarnocai, C., Canadell, J. G., Schuur, E. A. G., Kuhry, P., Mazhitova, G., and Zimov, S.: Soil organic carbon pools in the northern circumpolar permafrost region, Global Biogeochem. Cy., 23, n/a-n/a, 10.1029/2008gb003327, 2009.

Walter Anthony, K. and MacIntyre, S.: Noctural escape route for marsh gas, Nature, 535, 363–365, 10.1038/535363a, 2016.

Walter, K. M., Zimov, S. A., Chanton, J. P., Verbyla, D., and Chapin, F. S.: Methane bubbling from Siberian thaw lakes as a positive feedback to climate warming, Nature, 443, 71-75, 10.1038/nature05040, 2006.

Wang, L., Du, Z., Wei, Z., Xu, Q., Feng, Y., Lin, P., Lin, J., Chen, S., Qiao, Y., and Shi, J.: High methane emissions from thermokarst lakes on the Tibetan Plateau are largely attributed to ebullition fluxes, Sci. Total Environ., 801, 149692, 10.1016/j.scitotenv.2021.149692, 2021.

Wanninkhof, R.: Relationship between wind speed and gas exchange over the ocean revisited, Limnol. Oceanogr.-Meth., 12, 351-362, 10.4319/lom.2014.12.351, 2014.

Wik, M., Crill, P. M., Varner, R. K., and Bastviken, D.: Multiyear measurements of ebullitive methane flux from three subarctic lakes, J. Geophys. Res.-Biogeosciences, 118, 1307-1321, 10.1002/jgrg.20103, 2013.

Wik, M., Crill, P. M., Bastviken, D., Danielsson, Å., and Norbäck, E.: Bubbles trapped in arctic lake ice: Potential implications for methane emissions, J. Geophys. Res.-Biogeosciences, 116, G03044, 10.1029/2011JG001761, 2011.

Wik, M., Varner, R. K., Anthony, K. W., MacIntyre, S., and Bastviken, D.: Climate-sensitive northern lakes and ponds are critical components of methane release, Nat. Geosci., 9, 99-106, 10.1038/Ngeo2578, 2016.

Wik, M., Thornton, B. F., Bastviken, D., MacIntyre, S., Varner, R. K., and Crill, P. M.: Energy input is primary controller of methane bubbling in subarctic lakes, Geophys. Res. Lett., 41, 555-560, 10.1002/2013GL058510, 2014.

Yang, G., Zheng, Z., Abbott, B. W., Olefeldt, D., Knoblauch, C., Song, Y., Kang, L., Qin, S., Peng, Y., and Yang, Y.: Characteristics of methane emissions from alpine thermokarst lakes on the Tibetan Plateau, Nat. Commun., 14, 3121, 10.1038/s41467-023-38907-6, 2023.

Zabelina, S. A., Shirokova, L. S., Klimov, S. I., Chupakov, A. V., Lim, A. G., Polishchuk, Y. M., Polishchuk, V. Y., Bogdanov, A. N., Muratov, I. N., Guerin, F., Karlsson, J., and Pokrovsky, O. S.: Carbon emission from thermokarst lakes in NE European tundra, Limnol. Oceanogr., 66, S216–S230, 10.1002/lno.11560, 2020.

Zhao, F., Huang, Z., Wang, Q., Wang, X., Wang, Y., Zhang, Q., He, W., and Tong, Y.: Seasonal pattern of diel variability of CO_2 efflux from a large eutrophic lake, J. Hydrol., 645, 132259, 10.1016/j.jhydrol.2024.132259, 2024.

Page 10: [1] Deleted	**Amelie Pouliot**	**6/6/25 10:48:00 AM**
Page 10: [2] Deleted	**Amelie Pouliot**	**6/27/25 1:02:00 PM**
Page 10: [2] Deleted	**Amelie Pouliot**	**6/27/25 1:02:00 PM**
Page 10: [2] Deleted	**Amelie Pouliot**	**6/27/25 1:02:00 PM**
Page 10: [2] Deleted	**Amelie Pouliot**	**6/27/25 1:02:00 PM**
Page 10: [2] Deleted	**Amelie Pouliot**	**6/27/25 1:02:00 PM**
Page 10: [2] Deleted	**Amelie Pouliot**	**6/27/25 1:02:00 PM**
Page 10: [2] Deleted	**Amelie Pouliot**	**6/27/25 1:02:00 PM**
Page 10: [2] Deleted	**Amelie Pouliot**	**6/27/25 1:02:00 PM**
Page 10: [2] Deleted	**Amelie Pouliot**	**6/27/25 1:02:00 PM**
Page 10: [2] Deleted	**Amelie Pouliot**	**6/27/25 1:02:00 PM**
Page 12: [3] Deleted	**Amelie Pouliot**	**6/27/25 1:15:00 PM**
Page 12: [3] Deleted	**Amelie Pouliot**	**6/27/25 1:15:00 PM**
Page 12: [4] Deleted	**Amélie Pouliot**	**6/25/25 4:17:00 PM**
Page 12: [4] Deleted	**Amélie Pouliot**	**6/25/25 4:17:00 PM**

Page 12: [5] Deleted	**Amelie Pouliot**	**6/13/25 11:44:00 AM**
Page 12: [5] Deleted	**Amelie Pouliot**	**6/13/25 11:44:00 AM**
Page 12: [6] Deleted	**Amélie Pouliot**	**6/25/25 4:19:00 PM**
Page 12: [6] Deleted	**Amélie Pouliot**	**6/25/25 4:19:00 PM**
Page 12: [6] Deleted	**Amélie Pouliot**	**6/25/25 4:19:00 PM**
Page 12: [7] Deleted	**Amelie Pouliot**	**6/13/25 11:47:00 AM**
Page 12: [7] Deleted	**Amelie Pouliot**	**6/13/25 11:47:00 AM**
Page 12: [7] Deleted	**Amelie Pouliot**	**6/13/25 11:47:00 AM**
Page 12: [7] Deleted	**Amelie Pouliot**	**6/13/25 11:47:00 AM**
Page 12: [8] Deleted	**Amélie Pouliot**	**6/29/25 10:48:00 PM**
Page 12: [8] Deleted	**Amélie Pouliot**	**6/29/25 10:48:00 PM**
Page 12: [9] Deleted	**Amélie Pouliot**	**6/25/25 4:10:00 PM**
Page 12: [9] Deleted	**Amélie Pouliot**	**6/25/25 4:10:00 PM**
Page 12: [9] Deleted	**Amélie Pouliot**	**6/25/25 4:10:00 PM**
Page 12: [9] Deleted	**Amélie Pouliot**	**6/25/25 4:10:00 PM**
Page 12: [9] Deleted	**Amélie Pouliot**	**6/25/25 4:10:00 PM**
Page 12: [9] Deleted	**Amélie Pouliot**	**6/25/25 4:10:00 PM**

Page 12: [10] Deleted **Amelie Pouliot** **6/13/25 12:47:00 PM**

Page 12: [10] Deleted **Amelie Pouliot** **6/13/25 12:47:00 PM**

Page 12: [11] Formatted **Amélie Pouliot** **6/25/25 4:23:00 PM**

Font: Italic

Page 12: [11] Formatted **Amélie Pouliot** **6/25/25 4:23:00 PM**

Font: Italic

Page 12: [11] Formatted **Amélie Pouliot** **6/25/25 4:23:00 PM**

Font: Italic

Page 12: [12] Deleted **Amélie Pouliot** **6/13/25 3:59:00 PM**

Page 12: [12] Deleted **Amélie Pouliot** **6/13/25 3:59:00 PM**

Page 12: [12] Deleted **Amélie Pouliot** **6/13/25 3:59:00 PM**

Page 12: [12] Deleted **Amélie Pouliot** **6/13/25 3:59:00 PM**

Page 12: [12] Deleted **Amélie Pouliot** **6/13/25 3:59:00 PM**

Page 12: [12] Deleted **Amélie Pouliot** **6/13/25 3:59:00 PM**

Page 12: [13] Deleted **Amélie Pouliot** **6/20/25 3:08:00 PM**

Page 12: [13] Deleted **Amélie Pouliot** **6/20/25 3:08:00 PM**

Page 12: [13] Deleted **Amélie Pouliot** **6/20/25 3:08:00 PM**

Page 12: [13] Deleted **Amélie Pouliot** **6/20/25 3:08:00 PM**

Page 12: [13] Deleted	**Amélie Pouliot**	**6/20/25 3:08:00 PM**
Page 12: [13] Deleted	**Amélie Pouliot**	**6/20/25 3:08:00 PM**
Page 12: [13] Deleted	**Amélie Pouliot**	**6/20/25 3:08:00 PM**
Page 12: [14] Deleted	**Amélie Pouliot**	**6/20/25 3:24:00 PM**
Page 12: [14] Deleted	**Amélie Pouliot**	**6/20/25 3:24:00 PM**
Page 14: [15] Deleted	**Amelie Pouliot**	**6/27/25 1:24:00 PM**
Page 18: [16] Deleted	**Amelie Pouliot**	**6/6/25 10:50:00 AM**
Page 21: [17] Deleted	**Amelie Pouliot**	**6/6/25 10:51:00 AM**